



HAL
open science

The structures, stratigraphy and evolution of the Gulf of Corinth rift, Greece

Brian Taylor, Jonathan R. Weiss, Andrew M. Goodliffe, Maria Sachpazi,
Mireille Laigle, Alfred Hirn

► **To cite this version:**

Brian Taylor, Jonathan R. Weiss, Andrew M. Goodliffe, Maria Sachpazi, Mireille Laigle, et al.. The structures, stratigraphy and evolution of the Gulf of Corinth rift, Greece. *Geophysical Journal International*, 2011, 185 (3), pp.1189 - 1219. 10.1111/j.1365-246X.2011.05014.x . hal-01399970

HAL Id: hal-01399970

<https://hal.science/hal-01399970>

Submitted on 21 Nov 2016

HAL is a multi-disciplinary open access archive for the deposit and dissemination of scientific research documents, whether they are published or not. The documents may come from teaching and research institutions in France or abroad, or from public or private research centers.

L'archive ouverte pluridisciplinaire **HAL**, est destinée au dépôt et à la diffusion de documents scientifiques de niveau recherche, publiés ou non, émanant des établissements d'enseignement et de recherche français ou étrangers, des laboratoires publics ou privés.

The structures, stratigraphy and evolution of the Gulf of Corinth rift, Greece

Brian Taylor,¹ Jonathan R. Weiss,¹ Andrew M. Goodliffe,² Maria Sachpazi,³ Mireille Laigle⁴ and Alfred Hirn⁴

¹Department of Geology and Geophysics, School of Ocean and Earth Science and Technology, University of Hawaii at Manoa, Honolulu, HI, USA.
E-mail: taylorb@hawaii.edu

²Department of Geological Sciences, The University of Alabama, Tuscaloosa, AL, USA

³Geodynamic Institute, National Observatory of Athens, Athens, Greece

⁴Laboratoire de Sismologie Expérimentale, Département de Sismologie, Institut de Physique du Globe de Paris, Paris, France

Accepted 2011 March 8. Received 2011 February 10; in original form 2010 November 24

SUMMARY

A multichannel seismic and bathymetry survey of the central and eastern Gulf of Corinth (GoC), Greece, reveals the offshore fault geometry, seismic stratigraphy and basin evolution of one of Earth's most active continental rift systems. Active, right-stepping, en-echelon, north-dipping border faults trend ESE along the southern Gulf margin, significantly overlapping along strike. The basement offsets of three (Akrata-Derveni, Sithas and Xylocastro) are linked. The faults are biplanar to listric: typically intermediate angle ($\sim 35^\circ$ in the centre and $45\text{--}48^\circ$ in the east) near the surface but decreasing in dip and/or intersecting a low- or shallow-angle ($15\text{--}20^\circ$ in the centre and $19\text{--}30^\circ$ in the east) curvi-planar reflector in the basement. Major S-dipping border faults were active along the northern margin of the central Gulf early in the rift history, and remain active in the western Gulf and in the subsidiary Gulf of Lechaio, but unlike the southern border faults, are without major footwall uplift. Much of the eastern rift has a classic half-graben architecture whereas the central rift has a more symmetric w- or u-shape. The narrower and shallower western Gulf that transects the $>40\text{-km}$ -thick crust of the Hellenides is associated with a wider distribution of overlapping high-angle normal faults that were formerly active on the Peloponnese Peninsula. The easternmost sector includes the subsidiary Gulfs of Lechaio and Alkyonides, with major faults and basement structures trending NE, E–W and NW. The basement faults that control the rift architecture formed early in the rift history, with little evidence (other than the Vrachonisida fault along the northern margin) in the marine data for plan view evolution by subsequent fault linkage. Several have maximum offsets near one end. Crestal collapse graben formed where the hanging wall has pulled off the steeper onto the shallower downdip segment of the Derveni Fault. The dominant strikes of the Corinth rift faults gradually rotate from $090\text{--}120^\circ$ in the basement and early rift to $090\text{--}100^\circ$ in the latest rift, reflecting a $\sim 10^\circ$ rotation of the opening direction to the 005° presently measured by GPS. The sediments include a (locally $>1.5\text{-km}$ -) thick, early-rift section, and a late-rift section (also locally $>1.5\text{-km}$ -thick) that we subdivide into three sequences and correlate with seven 100-ka glacio-eustatic cycles. The Gulf depocentre has deepened through time (currently >700 mbsl) as subsidence has outpaced sedimentation. We measure the minimum total horizontal extension across the central and eastern Gulf as varying along strike between 4 and 10 km, and estimate full values of 6–11 km. The rift evolution is strongly influenced by the inherited basement fabric. The regional NNW structural fabric of the Hellenic nappes changes orientation to ESE in the Parnassos terrane, facilitating the focused north-south extension observed offshore there. The basement-penetrating faults lose seismic reflectivity above the 4–14-km-deep seismogenic zone. Multiple generations and dips of normal faults, some cross-cutting, accommodate extension beneath the GoC, including low-angle ($15\text{--}20^\circ$) interfaces in the basement nappes. The thermally cool forearc setting and cross-orogen structures unaccompanied by magmatism make this rift a poor analogue and unlikely precursor for metamorphic core complex formation.

Key words: Seismicity and tectonics; Continental tectonics: extensional; Sedimentary basin processes; Neotectonics; Fractures and faults.

1 INTRODUCTION

The Gulf of Corinth (GoC), which separates the Peloponnesus Peninsula from central Greece (Fig. 1), is one of the most active continental rift systems on Earth (Abers 2001) and therefore a much-studied natural laboratory of continental extension. For several reasons, however, interpretations of its structure, stratigraphy and basin evolution vary greatly and opposing conclusions have been reached regarding fundamental rift processes. One reason for this is the unusual tectonic setting of the GoC, obliquely transecting

the Hellenic forearc and mountains (Fig. 1). A second reason is that the GoC's laterally bounding structures have been hard to define, which typifies the overall lack of continuity of active structures linking the Anatolian strike-slip faults in the Aegean through central Greece to the Kefalonia Transform Fault and Ionian subduction system (McKenzie 1978; Le Pichon *et al.* 1995; Goldsworthy *et al.* 2002). A third reason is that none of the associated large earthquakes and only one of their aftershock sequences have been recorded by a seismometer array sufficiently densely spaced to resolve the controlling fault geometry (Bernard *et al.* 1997). A fourth reason is

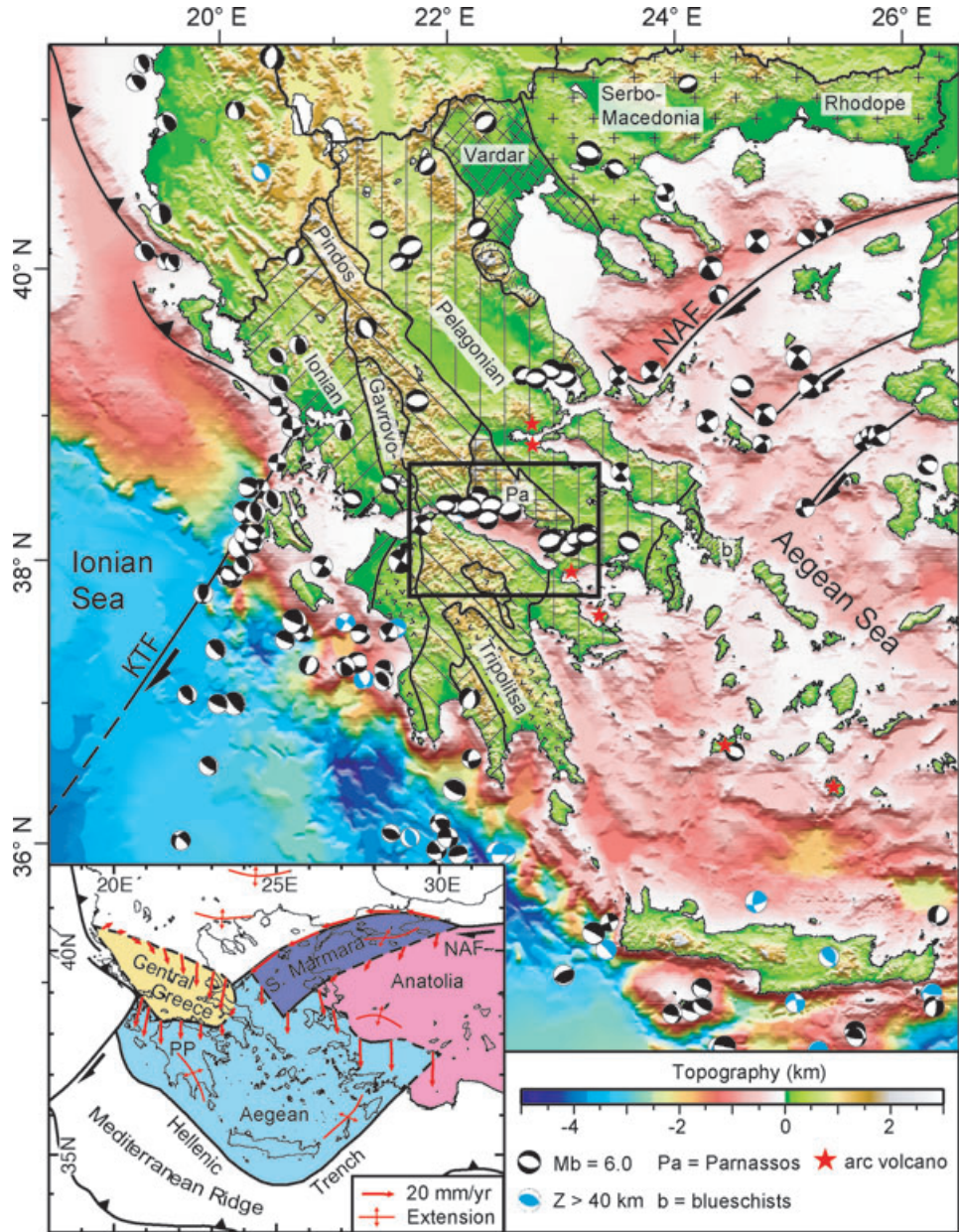


Figure 1. Topography, tectonics and geology of the Aegean region showing recent seismicity (1964–present) and arc volcanoes (red stars). Focal mechanisms of earthquakes are from the Harvard CMT catalogue and Kiratzi & Louvari (2003). Events >40 km deep have blue compression regions whereas those <40 km have black compression regions. Most of the deep earthquakes are subduction related. Named and patterned geologic units on the Greek mainland are after Hinsbergen *et al.* (2005), Jacobshagen *et al.* (1978), Jolivet *et al.* (2004) and Piper (2006). The black box indicates the area around and including the Gulf of Corinth shown in detail in Fig. 2. Inset map shows the four proposed continental microplates, interplate velocities (red arrows), and zones of internal extension/deformation from Nyst & Thatcher (2004). Deformation occurs primarily at the microplate boundaries although some of these, like the northern boundary of the Central Greece microplate, are poorly defined by active faults. The southern boundary of the Central Greece microplate is the Gulf of Corinth rift. KTF, Kefalonia transform fault; NAF, Northern Anatolian fault; PP, Peloponnesus Peninsula.

that the extension is focused offshore, beneath nearly 1 km of water and as much as 3 km of sediments. To penetrate this mask, image the active structures at depth, and distinguish between the various deformation models, we conducted a swath bathymetry and marine multichannel seismic (MCS) survey of the GoC. We interpret these and previous results to analyse the fault geometry, seismic stratigraphy, and basin evolution, and relate them to the regional tectonics. We find that the rift evolution is influenced greatly by the inherited basement fabric, with multiple generations and dips of normal faults, including low-angle ($15\text{--}20^\circ$) faults, accommodating extension in the Hellenic nappe stack beneath the GoC.

2 GEOLOGICAL AND TECTONIC SETTING

Mesozoic–Palaeogene convergence of the African and Eurasian Plates created alpine mountain ranges on the northern Mediterranean margin, including thickened crust in the Aegean and a stack of NNW-trending nappes in mainland Greece (Aubouin *et al.* 1970; Jacobshagen *et al.* 1978; Pe-Piper & Piper 2002). The Ionian and Gavrovo-Tripolitsa nappes, remnants of the continental margin of the African promontory of Apulia, underlie the Pindos nappe

whose strata (including Jurassic–Cretaceous pelagic carbonates and Paleocene flysch) formed in one of the oceanic seaways of Neotethys bordering the Pelagonian microcontinent (Fig. 1). The Hellenide orogen consumed ocean basins (Pindos and Vardar) in the Mesozoic and with their final closure, westward nappe stacking and major continental collisional uplift occurred in the early Tertiary (Aubouin *et al.* 1970; Jacobshagen *et al.* 1978; Pe-Piper & Piper 2002). The Parnassos is a large shallow-water carbonate platform (upper Triassic through Cretaceous) unit that lies between the Pindos and Pelagonian nappes, with deeper slope facies in its lower thrust sheets (Papanikolaou *et al.* 2009; Papastamatiou & Tataris 1963). The generally NNW structural fabric of the Hellenic nappe stack is aligned ESE uniquely in the Parnassos, pre-conditioning the structural grain of the basement of the central and eastern GoC (Fig. 2).

A strong reduction in the absolute motion of Africa towards Eurasia ~ 30 Ma, increasing retreat of the Tethyan slab (of which the Ionian Sea is an unsubducted remnant), and gravitational collapse of over thickened crust (Le Pichon *et al.* 1995) resulted in extension of the upper (Eurasian) plate and produced primarily arc-parallel basins in the Aegean until late Miocene time (Mercier *et al.* 1989; Jolivet & Faccenna 2000; Jolivet *et al.* 2010). This backarc-style extension was reorganized in the Pliocene associated with the SW

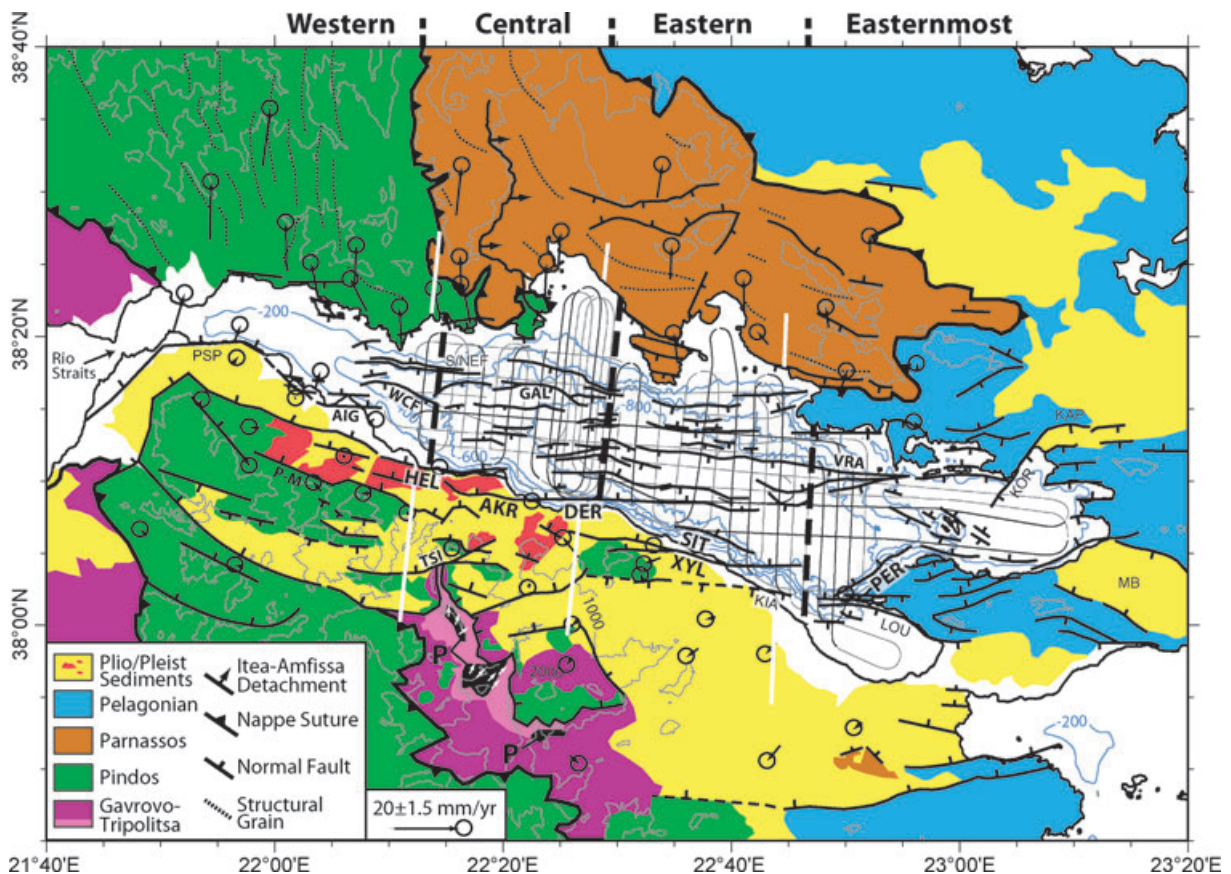


Figure 2. Geologic and fault map of the Gulf of Corinth and surrounding areas compiled from Bell *et al.* (2008), Flotte *et al.* (2005), Ford *et al.* (2007), Jolivet *et al.* (2010), Skourlis & Doutsos (2003), Palyvos *et al.* (2010), Papanikolaou *et al.* (2009), Schwan (1978) and references therein. Offshore faults within the grid of EW0108 MCS data (thin black lines) and GoC sector boundaries (thick dashed black lines) are from this study. Topography contour interval is 1000 m and bathymetry contour interval is 200 m. Also shown are GPS velocity vectors with uncertainty ellipses in a ‘Peloponnesus-fixed’ reference frame from Avallone *et al.* (2004). Vertical white lines are the locations of the profiles shown in Fig. 14. AIG, Aigion fault; P-M, Pirgaki-Mamousia fault; AKR, Akrata fault; DER, Derveni fault; GAL, Galaxidi fault; HEL, Heliki fault; KAP, Kaparelli fault; KIA, Kiato fault; KOR, Korombili fault; LOU, Loutraki fault; PER, Perahora fault; PSP, Psathopyrgos fault; S/NEF, S and N Eratini faults; SIT, Sithas fault; TSI, Tsvilos fault; VRA, Vrachonisida fault; WCF, West Channel Fault; XYL, Xylocaastro fault; MB, Megara Basin; P, Phyllite-Quartzite unit, with white arrows depicting shear directions from stretching lineations (Jolivet *et al.* 2010).

propagation of the Northern Anatolian Fault into the Aegean at $\sim 2\text{--}3$ Ma (Taymaz *et al.* 1991), faster slab roll-back, re-activation of some segments of the earlier formed rift zones (Armijo *et al.* 1996), and creation of new rift zones in central Greece and western Anatolia (Papanikolaou & Royden 2007). Global Positioning System (GPS) measurements reveal that the former pattern of regional Aegean extension has been replaced with coherent motion of the central and southern Aegean towards the SW at 30 ± 1 mm yr $^{-1}$ relative to Eurasia (McClusky *et al.* 2000).

Present-day Aegean deformation is associated dominantly with the relative motions of four microplates (Aegean, Central Greece, South Marmara and Anatolia) plus some straining in isolated zones internal to them, notably in the SE Aegean and southern Peloponnesus forearcs (Fig. 1 inset; Nyst & Thatcher 2004). In detail, the microplate motions are more complex than can be produced by simple models that combine slab roll-back, Northern Anatolian Fault propagation, and crustal collapse; note the roll-back-bounding Kefalonia Transform Fault terminating in the Central Greece microplate, for example. Although the continental deformation is concentrated on the microplate boundaries, some of these remain poorly defined by active faults, particularly the northern and eastern boundaries of the Central Greece microplate (Goldsworthy *et al.* 2002). In contrast, the southern boundary of the Central Greece microplate is precisely the GoC rift, where geodetic data show that the active extension is focused offshore. GPS stations on the northern Peloponnesus are not moving relative to one another, whereas the displacement

rate of stations north of the GoC in central Greece increases from 11 mm yr $^{-1}$ adjacent Xylocastro to 16 mm yr $^{-1}$ adjacent Aigion, both along N005°E (Figs 2 and 3; Briole *et al.* 2000; Avallone *et al.* 2004), consistent with the rotation derived by Nyst & Thatcher (2004). On the Peloponnesus, only the three GPS stations located north of the southern GoC border faults west of Aigion share in the relative displacement, meaning that motion on the other northern Peloponnesus normal faults (Doutsos & Piper 1990; Armijo *et al.* 1996; Ghisetti & Vezzani 2004; Ghisetti & Vezzani 2005) has ceased or is below detection (< 1 mm yr $^{-1}$; Avallone *et al.* 2004). In contrast to these fast rates at present, GoC extension of 2–4 mm yr $^{-1}$ has been estimated from geological data averaged over late Quaternary times (Westaway 2002).

Both modern and historical (since 480 B.C.) seismicity attest to the activity of the GoC rift (Ambraseys & Jackson 1990; Hatzfeld *et al.* 2000). In the last 50 yr 11 normal fault earthquakes $M_b = 5.0\text{--}6.1$ shook the region surrounding the Gulf. In the west and centre, the 1965, 1970, 1992 and 1995 events were located at 7–10 km depth beneath the northern GoC margin and characterized by shallow, N-dipping nodal planes (23–34°) and steep S-dipping planes (Rigo *et al.* 1996; Fig. 3). In the easternmost sector, a 1981 cluster of events was located in and around the Alkyonides subbasin at 7–15 km depth, and characterized by nodal planes dipping $39^\circ \pm 10^\circ$ (Jackson *et al.* 1982; King *et al.* 1985; Taymaz 1992; Braunmiller & Nabelek 1996). Unfortunately, networks of seismometers with spatial densities approximating the hypocentral

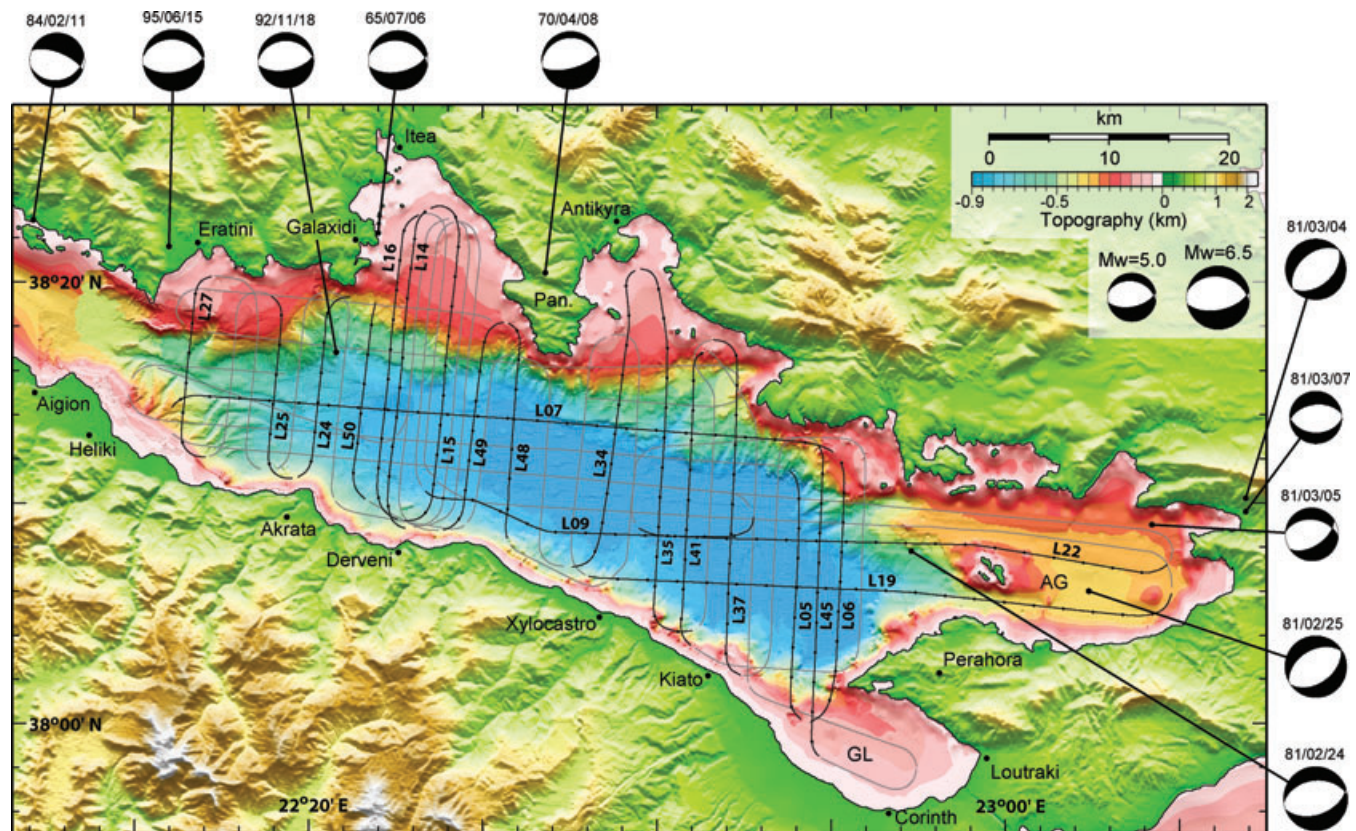


Figure 3. Multibeam bathymetric data collected in the Gulf of Corinth during EW0108 combined with bathymetry from the western Gulf from McNeil *et al.* (2005) and the digital elevation model of Greece. Light track lines show the locations of the MCS data collected during EW0108 and dark track lines are the data presented in Figs 4–10 of this paper. Focal mechanisms for major recent earthquakes are shown around the perimeter. Note the shallow-angle, north dipping nodal planes on the 1995, 1992, 1965 and 1970 earthquakes that occurred beneath the northern Gulf margin. Cross-sections of some of these earthquake focal mechanisms are shown in Fig. 14. Pan., Pangalos Peninsula; AG, Alkyonides Gulf; GL, Gulf of Lechaio.

depths were not deployed at the time of these earthquakes or their aftershocks to better resolve the controlling fault location and geometry; the exception being the study by Bernard *et al.* (1997) of the aftershocks of the 1995 Aigion earthquake that constrained slip to a fault nucleating under the north coast at 10 km depth and propagating up dip to the south at 33°. Such networks, deployed at other times, recorded micro-earthquakes including clusters that relocated along northward-dipping planes that have been cited as evidence for an active low-angle detachment beneath the western Gulf (Rietbrock *et al.* 1996; Rigo *et al.* 1996; Gautier *et al.* 2006). An analysis of refracted active-source seismic wave arrivals performed in parallel with this study confirms the presence of a shallow, northward-dipping interface beneath the southern margin of the central Gulf (Pi Alperin *et al.* 2004). Hatzfeld *et al.* (2000), however, suggest that the northward-dipping base of the microseismicity represents the brittle–ductile transition at 8–12 km depth and not an active low-angle fault. Intense fluid circulation in the shallow sediments and karstified limestones has complicated heat flow measurements in the region. The one exception is the heat flow of 53 mW m⁻² derived from temperature and thermal conductivity measurements above the Aigion fault that was intersected at 760–770 m in the 1000-m-deep AIG10 borehole (Doan & Cornet 2007). The authors suggest that Corinth rifting has not significantly elevated the heat flow, whose value we note is consistent with a thermally cool forearc of orogenically thickened continental crust.

3 PHYSIOGRAPHY AND CRUSTAL STRUCTURE

The physiography of the GoC and its surrounds reflect the modification of the inherited geomorphology and crustal structure by extension tectonics and sedimentation/erosion. Distributed Miocene arc/backarc extension thinned Aegean crust to ~25 km thick whereas the crustal backbone of the Hellenic mountains beneath the Pindos and Gravrovo-Tripolitsa nappes (Fig. 1) exceeds 40 km thickness (Makris 1978; Papazachos & Nolet 1997; Tiberi *et al.* 2001; Le Pourhiet *et al.* 2003; Clement *et al.* 2004; Zelt *et al.* 2005; Sachpazi *et al.* 2007). The GoC obliquely transects these terranes, from the 25-km-thick crust beneath the Perahora Peninsula (Zelt *et al.* 2005) across the Hellenic mountains and through the ≤65-m-deep Rio Straits to the Ionian Sea of the Mediterranean (Figs 1–3). The GoC is <400 m deep west of Aigion, and has subsidiary Gulfs of Itea and Antikyra in the north (<100 m depth), Alkyonides in the east (<200 m) and Lechaio in the SE (<100 m; Fig. 3).

The 700 m isobath approximately outlines the modern depocentre of the central and eastern GoC, the near-planar floor of which is at depths of 800–880 m (Figs 2 and 3). Sediment is delivered from all sides: the low-relief northern margin, the Gulfs of Alkyonides and Lechaio in the east and SE, the high-relief southern margin, and by an axial and tributary channels from the shallower western basin, but particularly from the south and west. Prograding fan deltas, and sea level change and seismically induced mass gravity movements, are primary sedimentary processes on the steep gulf flanks (Heezen *et al.* 1966; Ferentinos *et al.* 1988; Papatheodorou & Ferentinos 1997; Lykousis *et al.* 1998; Lykousis *et al.* 2007). The submarine slopes, between the shelves and basin floor, are heavily dissected by channels and canyons, most of which have no continuation on the surrounding shelves or land (Fig. 3). There are two exceptions to this generality. The first are those submarine channels/canyons whose courses are influenced/controlled by faults, such as at the mouths of the Gulfs of Lechaio, Alkyonides and SE Antikyra, and the western

axial channel (compare Figs 2 and 3). The second results from the rivers that originate many kilometres south of the Peloponnesus coastline, predate the current border fault configuration, maintain their courses and incise canyons on the uplifted footwall slopes of the active border faults (Goldsworthy & Jackson 2001) (Fig. 3). Uplift of the Heliki fault footwall, however, redirected flow of the Kratis River towards the ramp between the en echelon Heliki and Derveni faults (Weiss 2004; Ford *et al.* 2007; Fig. 2).

Differential subsidence between the western and central GoC has led to submarine channels incising the slope between the western basin floor (which is above 400 m depth) and the central basin floor (which is below 700 m depth, Fig. 3). There is an axial channel, whose course is controlled by the S-dipping West Channel Fault (Bell *et al.* 2008), with pinnate tributary channels in its middle and upper reaches and sinuous channels that subparallel its lower reach, coming NE off the foot of the southern slope of the basin and then turning easterly. The slope between the west and central GoC floor (north of Heliki and Akrata, Fig. 3) correlates with a westward-thickening crust (Zelt *et al.* 2005; Sachpazi *et al.* 2007), a NNW-trending basement culmination that Ghisetti & Vezzani (2005) infer formed by upper crustal doming during Miocene extension, and the middle/late Miocene–early Pliocene East Peloponnesus Detachment System (EPDS) of Papanikolaou & Royden (2007), whose northern extent is the Itea-Amfissa detachment which trends north from Galaxidi parallel to the Pindos suture (Figs 2 and 3; Papanikolaou *et al.* 2009).

Regional uplift of the Peloponnesus and Perahora Peninsulas is revealed by fluvial incision and uplifted marine Plio-Quaternary sediments including the late Pleistocene Corinthian terraces on the south coast east of Xylocaastro (e.g. Philippson 1892; Keraudren & Sorel 1987; Collier *et al.* 1992; Armijo *et al.* 1996; Leeder *et al.* 2003; McNeil & Collier 2004; Leeder *et al.* 2005) and the Holocene and Pleistocene terraces at the eastern tip of the Heliki fault (McNeil & Collier 2004). Some have ascribed the regional uplift to forearc uplift above the shallowly dipping Hellenic subduction zone (Collier *et al.* 1992; Leeder & Mack 2007). The regional uplift is modulated by flexural uplift of fault footwalls and the northward propagation of normal fault activity towards the western Gulf (Ori 1989; Gawthorpe *et al.* 1994; Leeder *et al.* 2008). The maximum rates (~1.5 mm yr⁻¹, possibly increasing to ~3 mm yr⁻¹ in the Holocene) and amplitudes (~1600 m) of Quaternary uplift are located south of the central GoC (Akrata-Derveni, Fig. 3) and taper off from there to the east and west (Houghton *et al.* 2003; Pirazzoli *et al.* 2004).

4 METHODS AND PREVIOUS DATA

The MCS and multibeam bathymetry data presented here were collected during a geophysical survey aboard the R/V *Maurice Ewing* between 2001 July 23 and August 1 (EW0108) that included 33°N–S and 10°E–W trending lines (with azimuths of ~N005°E and ~N095°E, respectively, Figs 2 and 3). This was the first comprehensive deep-penetration MCS investigation of the submarine basin in the GoC. Prior to this survey some shallow-penetration, high-resolution seismic reflection data from the Gulf existed (Perissoratis *et al.* 1986; Lykousis *et al.* 1998; Sakellariou *et al.* 1998; Perissoratis *et al.* 2000; Stefatos *et al.* 2002) in addition to a few MCS profiles that did not image the basement (Brooks & Ferentinos 1984; Higgs 1988). In addition, Lykousis *et al.* (2007) and Sakellariou *et al.* (2007) collected a dense grid of shallow-penetration MCS data across the entire Gulf, and McNeil *et al.* (2005) and Bell *et al.* (2008) did likewise for the region offshore

Aigion and Helike, but these profiles image the upper portion of the sediment section and the basement only along the Gulf margins. Clement (2000) pre-stack depth migrated two cross-basin MCS profiles shot for DEP-Hellenic Petroleum and one along-basin French-Greek SEIS-GREECE 1997 profile that provided the first images penetrating into the basement (Sachpazi *et al.* 2003).

For the EW0108 survey, a 20 air gun, 8445 cu. in. array was used as a seismic source with a shot interval of 50 m. For each shot, 16 384 ms of data were recorded at a 4 ms sample rate. Easterly oriented lines and the longer N-S lines in the Gulf of Itea were shot using a 240-channel, 6-km-long streamer with a group interval of 25 m (L1–L23) whereas most of the other N–S lines were shot to a 240 channel, 3-km-long streamer, with a group interval of 12.5 m (L24–L50). The change in streamer length was a precautionary response to boat traffic, facilitated acquisition and reduced spatial aliasing of dipping structures on the N–S lines across the narrow axis of the Gulf. The streamer was instrumented with depth control birds (set to 10 m for this survey) with compasses that provided streamer depth and bearing. Navigation was recorded by GPS receivers on the tail-buoy and on the R/V *Maurice Ewing* and integrated with the seismic data in United Kingdom Offshore Operators Association (UKOOA) format. The data acquisition parameters were biased towards deep penetration, as was achieved using a 5-km streamer on the same vessel to image the shallow-dipping normal fault to >8 km in the Moresby Rift of the western Woodlark Basin (Taylor *et al.* 1999). All of the MCS data are archived at the UTIG Marine Seismic Data Center (www.ig.utexas.edu).

MCS data were processed through post-stack migration and interpreted at the University of Hawaii using ProMAX and SeisWorks, both Landmark Graphics Corporation products. Following is a brief description of the processing steps used to create the MCS images presented in this paper. A crooked-line binning method was used to geographically position each of the shots to preserve as much data as possible around turns near the Gulf margins. The data were edited for bad shots and excessively noisy channels. Refraction first arrivals were muted; predictive deconvolution was performed to compress the source wavelet; and a band pass filter was applied to reduce the low- and high-frequency noise signals boosted after deconvolution (Yilmaz 2001). The data were sorted into the common depth-point domain (CDP) using the crooked-line geometry of the streamer and a spacing of 25 m between CDP's. Velocity analysis was performed on selected groups of CDP gathers and spatially interpolated to apply a normal-moveout (NMO) correction. Top and inside mutes were applied to remove the excessively stretched data and to suppress the strong seafloor multiples, respectively. The data were stacked and a time-varying band pass filter pass was applied to further suppress the seafloor multiple. Finally, the data were migrated using the most satisfactory root mean square (RMS) velocities and interpreted in SeisWorks in the time domain. Only the top four seconds of the MCS data are presented in Figs 5–9 because no coherent reflections other than multiples were recognized below that.

Select MCS lines were also post-migration depth converted in ProMAX to better determine fault dip and sediment thickness. An average velocity of 1.5 km s^{-1} was used in the water and linear velocity gradients in time were determined for the sediment section and basement to create a velocity space for each MCS profile. The velocity used in the sediment section increased by $1 \text{ km s}^{-1} \text{ s}^{-1}$ from 1.5 km s^{-1} at the water-sediment interface to the top of the basement. The sediment thickness in the Gulf, and hence the maximum sediment velocity, is highly variable. The velocity used in the basement increased from 5 km s^{-1} by $0.25 \text{ km s}^{-1} \text{ s}^{-1}$. These simple

linear velocity gradients were derived from a synthesis of interval velocity models based on our NMO velocity analyses and streamer tomography of the EW0108 MCS data (Zelt *et al.* 2004), and pre-stack depth conversion of the DEP-Hellenic Petroleum MCS data (Clement 2000; Sachpazi *et al.* 2003).

Multibeam bathymetric data were collected during EW0108 using a Hydrosweep DS-2 multibeam sonar system and manually edited after sound-velocity corrections were applied using data from four XBT (salinity, depth and temperature) profiles collecting during the survey. The bathymetry data are gridded with a cell size of 0.0005° ($\sim 55 \text{ m}$) and include points digitized from nautical charts to fill data gaps in shallow portions of the Gulf. The data presented in Fig. 3 are a combination of the EW0108 bathymetry, those collected by McNeil *et al.* (2005) north of Aigion and Akkrata, and a digital elevation model (DEM) of Greece topography (Fig. 3). High-resolution swath bathymetry data have been published for the Alkyonides Gulf by Sakellariou *et al.* (2007).

5 SEISMIC STRATIGRAPHY

The basin fill sediments include a thick, early-rift section, and a late-rift section that we subdivide into three sequences and correlate with seven 100-ka glacio-eustatic cycles (Fig. 4). The early-rift section varies considerably in thickness across the Gulf and its lower part generally lacks distinct, high-amplitude, basin-wide reflectors. For this reason we treat the early-rift section as one depositional unit spanning a large time interval (mainly Early Pleistocene, see below), during which resolution and correlation of discrete tectono-sedimentary events is difficult. Areas of coherent, continuous horizons are present where the early-rift sequence is not too thick (such as near the intersection of L50, L16 and L14 with L02, Figs 5, 6, and in the east on L34–L06, Figs 7, 8). From locations such as these we infer that the early-rift sediment fill once consisted of continuous horizons but, due to intense faulting and fault rotation during and after early-rift deposition, much of this coherency has been destroyed in the thicker sections.

In contrast, the late-rift section is composed of numerous identifiable sequences that span the majority of the central and eastern basin. The sequences consist of alternating highly reflective units and semi-transparent units. The reflective units are composed of doublets or triplets of high-amplitude, continuous, parallel reflectors whereas the semi-transparent units are composed of low amplitude, continuous, parallel reflectors. Typically, the semi-transparent units are thicker than the highly reflective units although both change in thickness along and across the strike of major structures in the basin. To facilitate our interpretation and discussion of the evolution of the basin we subdivide the late-rift section into three major sequences numbered 1–3 from the early/late-rift transition to the seafloor (although clearly it is possible to further subdivide the late-rift section). Although their character varies along strike, the sequence boundaries are unconformities towards the basin margins and conformable with under- and overlying horizons across depocentres in the centre of the basin.

In the absence of drill-hole data from the sediment section, we follow previous workers (e.g. Gawthorpe *et al.* 1994; Perissoratis *et al.* 2000; Sachpazi *et al.* 2003) in proposing a correlation of the seismic sequences with the 100-ka glacio-eustatic cycles whose $\sim 120\text{-m}$ -amplitude transformed the gulf into a lake when sea level fell below the $\sim 65 \text{ m}$ sill depth of the Rio Straits (Fig. 2). Sea level cycles have been correlated on subaerial terraces south of the Gulf (e.g. Keraudren & Sorel 1987; Armijo *et al.* 1996; McNeil &

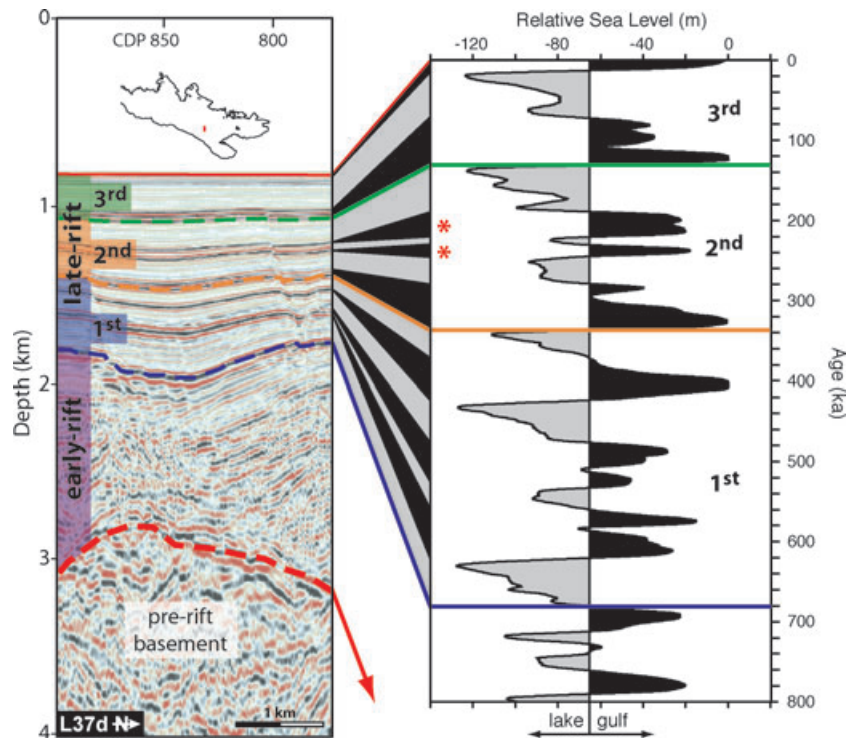


Figure 4. Seismic stratigraphy of a representative Gulf of Corinth depth section (L37) correlated with relative sea level for the past 800 ka from Bintanja & van de Wal (2008). We divide the sedimentary section into early versus late rift, and the latter into 1st, 2nd and 3rd sequences that correlate with seven 100-ka glacio-eustatic cycles. One of the characteristic reflectors is the basin-wide seismic doublet within late rift sequence 2 (double asterisk) that we correlate with the sea level highstands at ~200 and 240 ka.

Collier 2004) and have been recognized within the Gulf on shallow penetration seismic data and sediment cores (Lykousis *et al.* 1998; Perissoratis *et al.* 2000; McNeil & Collier 2004; Lykousis *et al.* 2007; Sakellariou *et al.* 2007; Bell *et al.* 2008; Bell *et al.* 2009). The basin-wide extent of the late-rift sequences and their cyclic nature indicates primary control by global sea level fluctuations rather than by discrete tectonic events (Sachpazi *et al.* 2003).

Fig. 4 shows our proposed correlations of a representative EW0108 seismic section to a reconstructed sea level curve (Bintanja & van de Wal 2008) for the past *ca.* 800 ka. We adopt the alternating marine and lacustrine sedimentation model of Leeder *et al.* (1998, 2005) and Collier *et al.* (2000), developed for the Alkyonides sub-basin and also used by Bell *et al.* (2008, 2009). In their model that links paleoclimate with seismic stratigraphic and shallow core data, glacial lacustrine periods are characterized by low-stand deltaic and paralic clinoforms and thick basin deposits, associated with higher sediment yields due to wet winters and steppe-like vegetation promoting high run-off in the absence of significant tree cover. Interglacial, gulf conditions are characterized by condensed sedimentary sections (thin, reflective, highstand deposits), associated with low sediment yields and arboreal forests.

A direct seismic correlation between the sediments of the Alkyonides or Eratini subbasins and the GoC basin is not possible because of the intervening Alkyonides Islands or Eratini horst basement highs (Figs 3 and 9). Nevertheless we adopt the model that the alternating seismic sequences imaged in the late-rift basin section probably record the many transitions from lacustrine (thick, semi-transparent) to marine (thin, highly reflective) conditions. Comparison of our inferred stratigraphy to the sea level curve (Fig. 4) lends credence to this interpretation. The cyclicity of seismic reflections is

well matched to the sea level curve, particularly for the past 500 ka, under the assumption of condensed highstand sections producing the stronger reflectors. For example, note the basin-wide seismic doublet within LRS 2 that we correlate with the sea level highstands at 200 and 240 ka. The alternative interpretation, that lowstand conditions produce the highly reflective units from turbidity currents of coarse grained, river-fed material (Perissoratis *et al.* 2000) would not produce the observed dominance in the thickness of acoustically weak versus strong units within the MCS data.

Using this model of highly reflective units recording slow deposition during sea level high stands (i.e. gulf conditions) and the semi-transparent units recording faster deposition during low stands (i.e. lake conditions), our correlation of the MCS data with the sea level curve (Fig. 4) places the 3rd/2nd LRS boundary at ~130 ka, the 2nd/1st LRS boundary at ~335 ka, and the early/late-rift boundary at ~680 ka. Our age assignments progressively diverge with depth from those proposed by Sachpazi *et al.* (2003), Lykousis *et al.* (2007) and Bell *et al.* (2008, 2009). We make the early-rift section older, notably increasing the inferred age of the early/late-rift boundary from ~480 to ~680 ka, in accord with data from the rift sections that crop out on the northern Peloponnesus (Ford *et al.* 2007). To test this difference will require drilling.

Onshore investigations from Heliki to Akkrata (Fig. 3) have identified three lithostratigraphic units including a Lower Group attributed to rift basin formation at ~3.6 Ma and a Middle Group following rapid basin deepening and lacustrine deposition at ~1.5 Ma (Ford *et al.* 2007; Rohais *et al.* 2007; Rohais *et al.* 2008). A major unconformity separating the Middle and Upper Groups represents a northward shift in dominant fault activity from the Pirgaki-Mamoussia fault (P-M in Fig. 2) to the Heliki fault at ~700 ka. The stepped

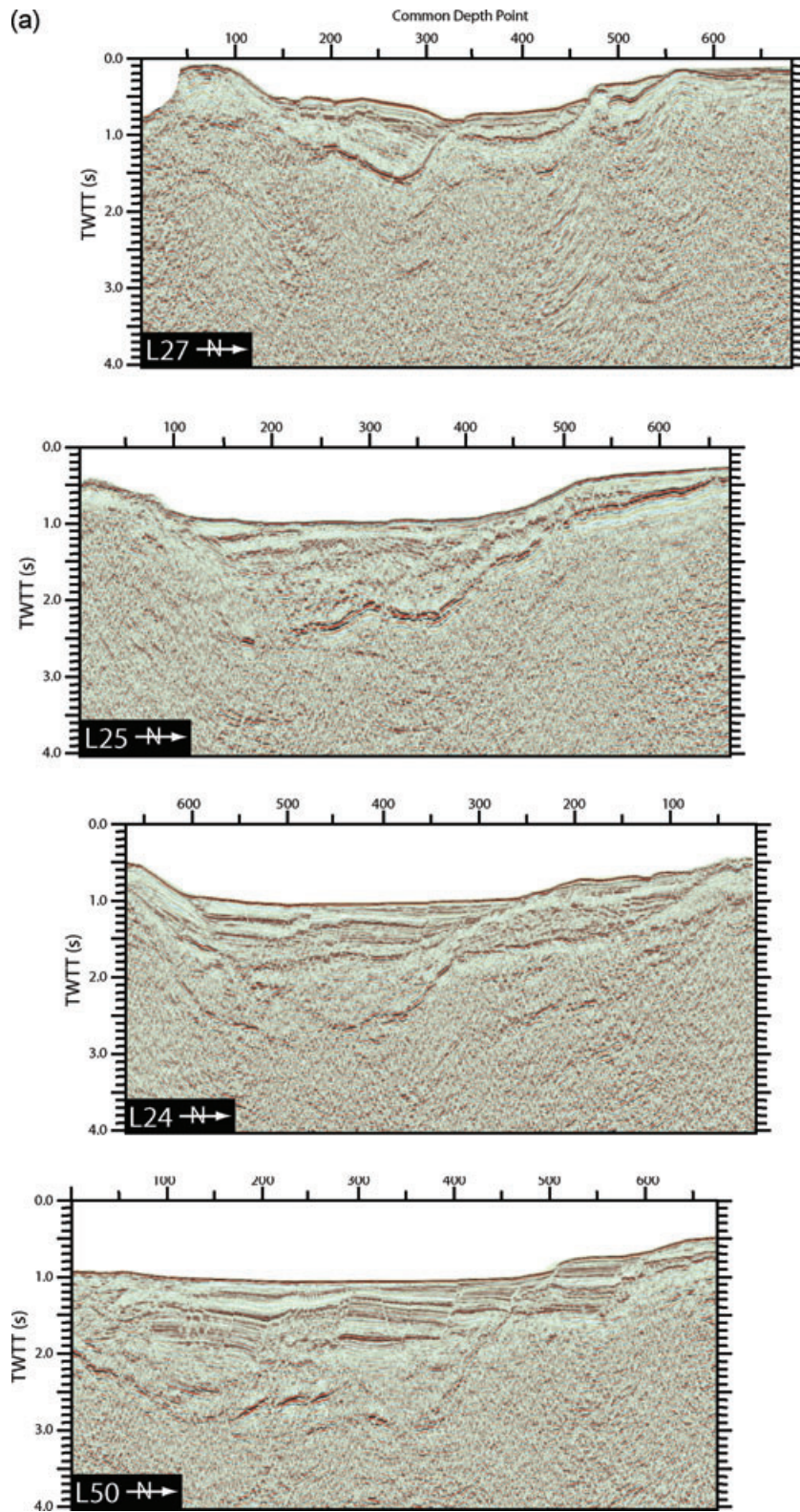


Figure 5. Representative (a) uninterpreted and (b) interpreted EW0108 MCS data from the western (L27) and central (L25, L24 and L50) sectors. H, Heliki fault; WCF, West Channel fault; S/NEF, S and N Eratini faults; ESB, Eratini subsbasin; GAL, Galaxidi fault; A-D, Akrata-Derveini fault; W, western sector; C, central sector.

terraces and slope breccia deposits of the Upper Group (*ca.* 0.7 Ma to present) south of the eastern tip of the Heliki fault and the active Gilbert fan deltas on the western portion of the Heliki fault are the onshore equivalents of the late-rift sequence. In our interpretation,

consistent with Ford *et al.* (submitted), the offshore early-rift section is equivalent to the Lower and Middle Groups, mainly the latter (*i.e.* Early Pleistocene). Deep early-rift strata with variably oriented dips in isolated fault-bounded depocentres and associated erosional

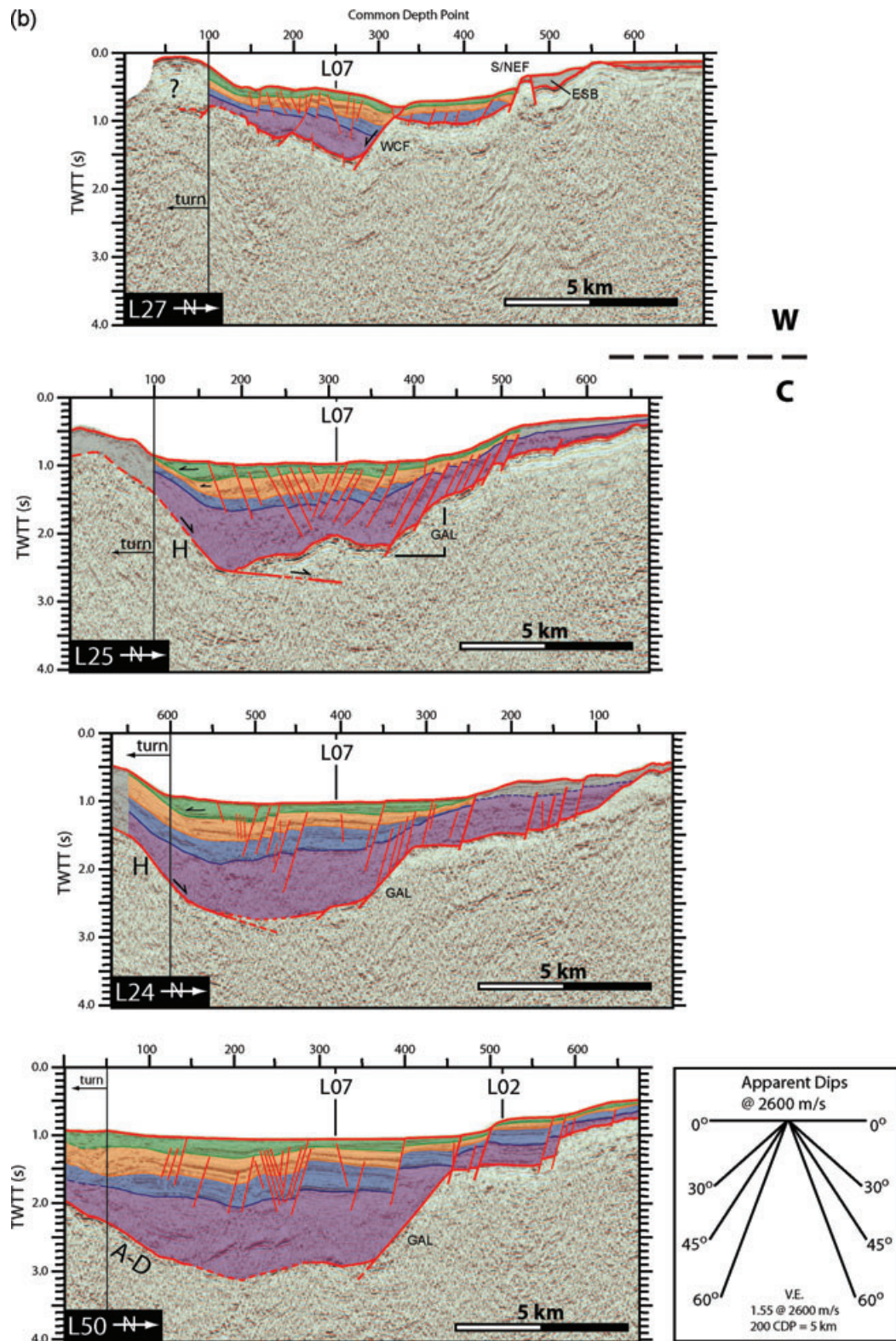


Figure 5. (Continued.)

unconformities are the offshore equivalent of Middle to Late Pliocene fluvio-lacustrine deposits found south of the western and central sectors (Lower Group) and in the Megara Basin (Ford *et al.* 2007; Leeder *et al.* 2008).

6 RIFT GEOMETRY AND EVOLUTION

The EW108 MCS data provide a comprehensive grid (Fig. 3) of 2-D images of the syn-rift sediments, basement and faults in the

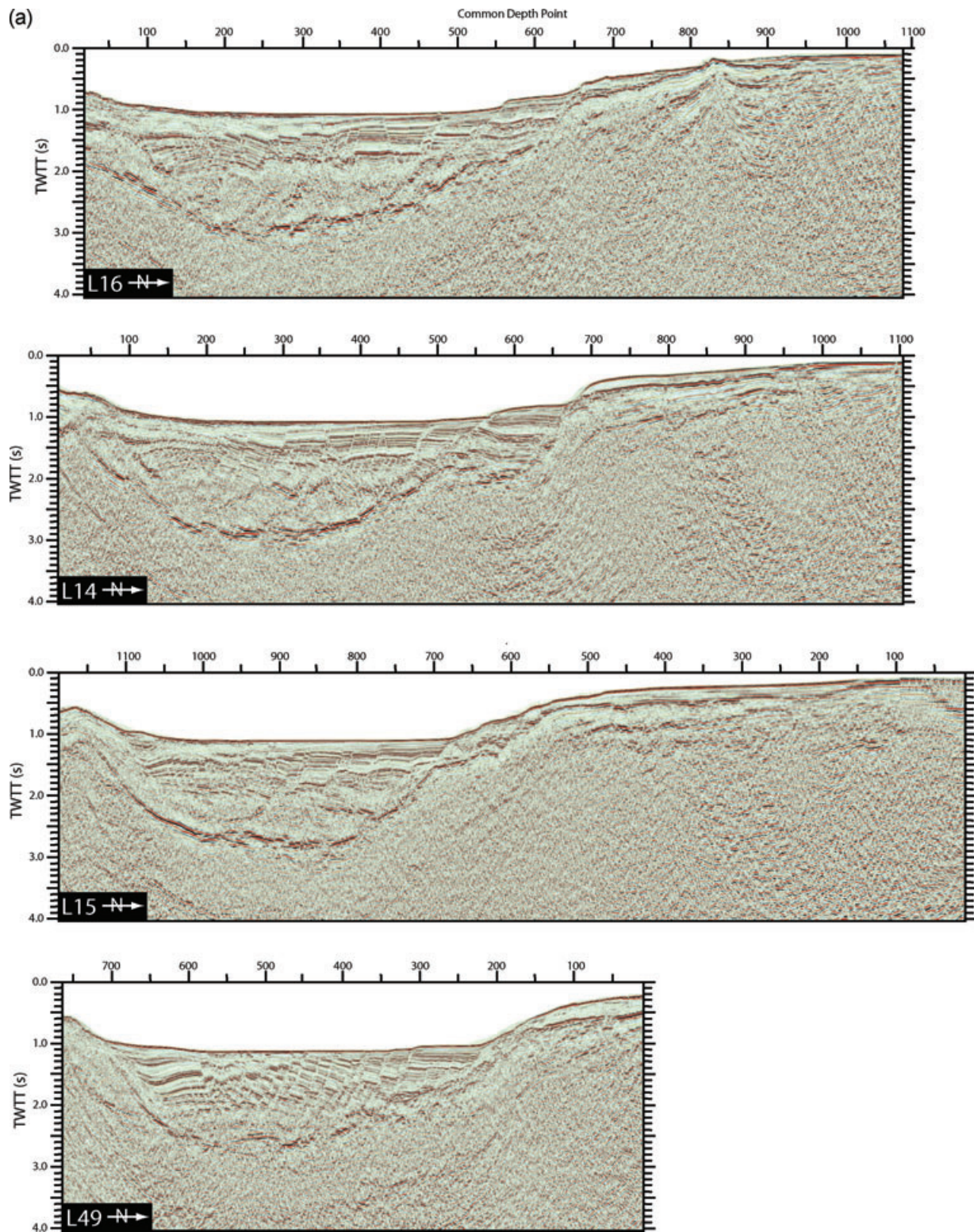


Figure 6. Representative (a) uninterpreted and (b) interpreted EW0108 MCS data from the central (L16, L14 and L15) and eastern (L49) sectors. D, Derveni fault; GAL, Galaxidi fault; C, central sector; E, eastern sector.

central and eastern GoC. We present a representative subset of the across (N–S; Figs 5–8) and along (E–W; Fig. 9) strike MCS lines to illustrate the varied GoC structural and stratal geometries. Post-migration, depth-converted MCS data provide dip information (Fig. 10).

The four seismic stratigraphic sequences shown in Fig. 4 were correlated across the EW0108 MCS dataset and used to create two-way traveltime sequence thickness (isopach, strictly ‘isochor’) and offsetting fault maps (Fig. 11). The faults shown cross at least two seismic lines and/or correspond to noticeable changes in

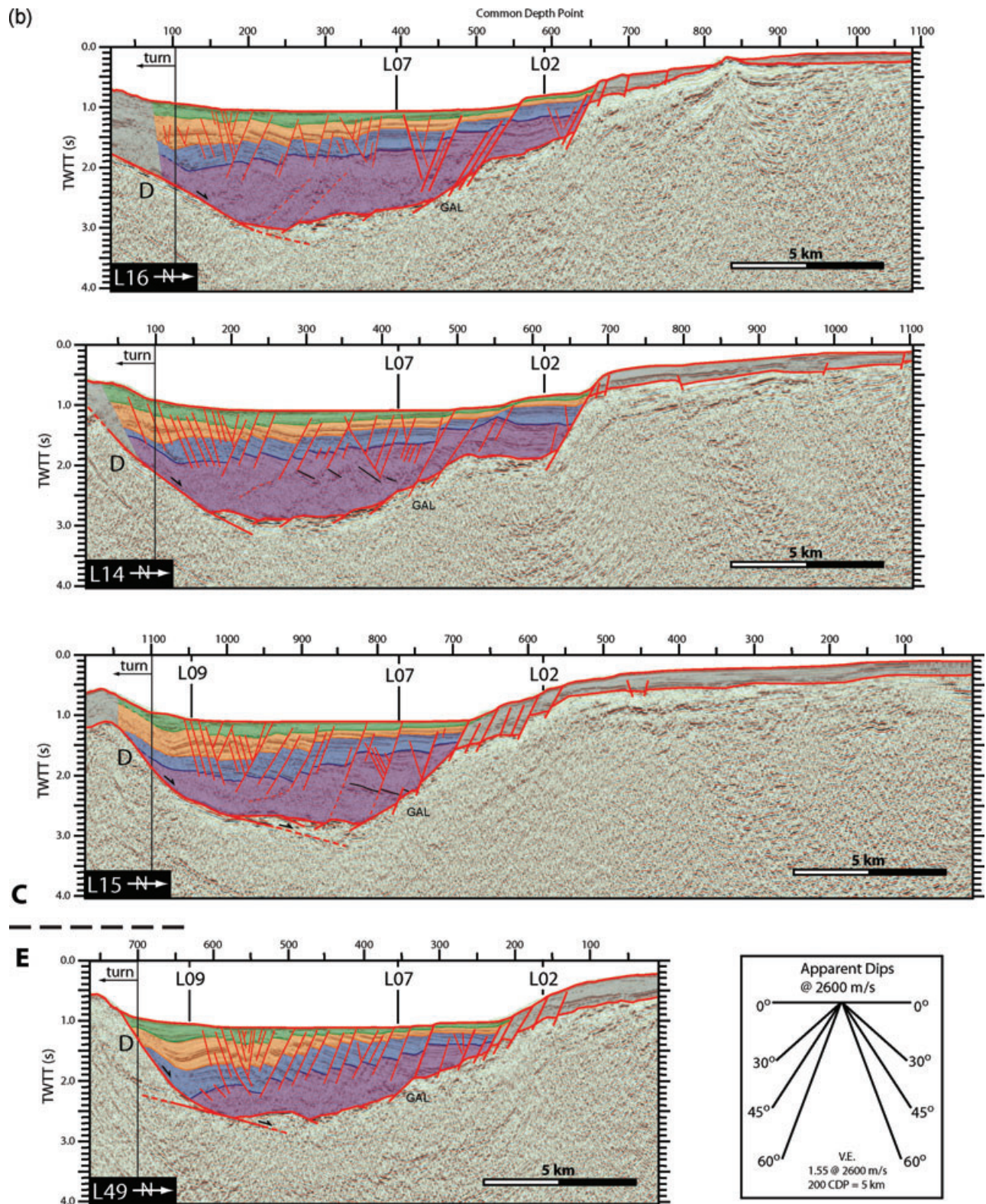


Figure 6. (Continued.)

sequence thickness. The widths of the fault polygons depict the area of intersection of each fault with that sequence. Thus, up section the fault locations migrate updip. In mapping the faults, care was taken to preserve structural and isopach contour trends. Nevertheless, survey line spacing typically >1 km makes it difficult

to uniquely correlate the numerous closely spaced minor faults in some areas of intense deformation of the syn-rift section.

Inspection of the bathymetry and MCS data (Figs 2, 5–10) reveals first-order differences in the surveyed portion of the GoC basin such that it may be subdivided it into at least four rift

(a)

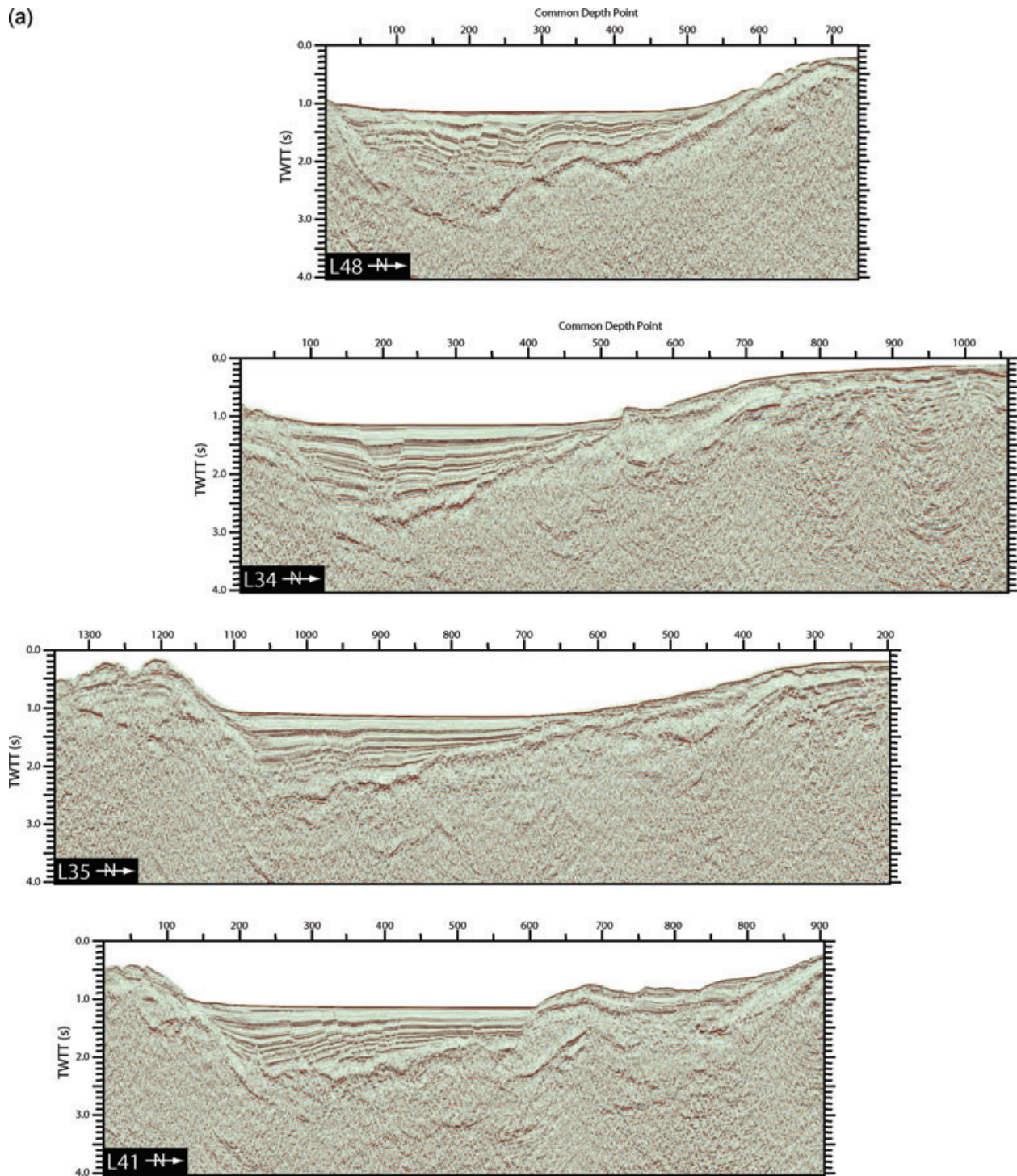


Figure 7. Representative (a) uninterpreted and (b) interpreted EW0108 MCS data from the eastern sector. S, Sithas fault; X, Xylocastro fault; DFG, Derveni fault graben; VRA, Vrachonisida fault.

sectors along strike (Fig. 12). The central sector has a w- or u-shaped geometry with controlling border faults to both the north (Galaxidi) and south (Helike and Derveni). The basin is an asymmetric graben or half-graben tilted to the south against the Derveni-Sithas-Xylocastro border faults in the eastern sector, and tilted to the north against the axial west channel fault in the western sector. The easternmost sector of Perahora-Lechaio-Alkyonides has several subbasins of varying geometries. The following description of the GoC rift geometry and evolution will proceed, by

sectors, from west to east and from bottom to top (i.e. basement to seafloor).

6.1 Western sector

In the western GoC rift sector, that transects the Hellenic mountain Pindos nappes (Figs 1 and 2), the seafloor is shallow (mostly <400 m, Figs 2 and 3) and the crust is thick (~40 km) (e.g. Zelt *et al.* 2005; Sachpazi *et al.* 2007). Our survey collected only one

(b)

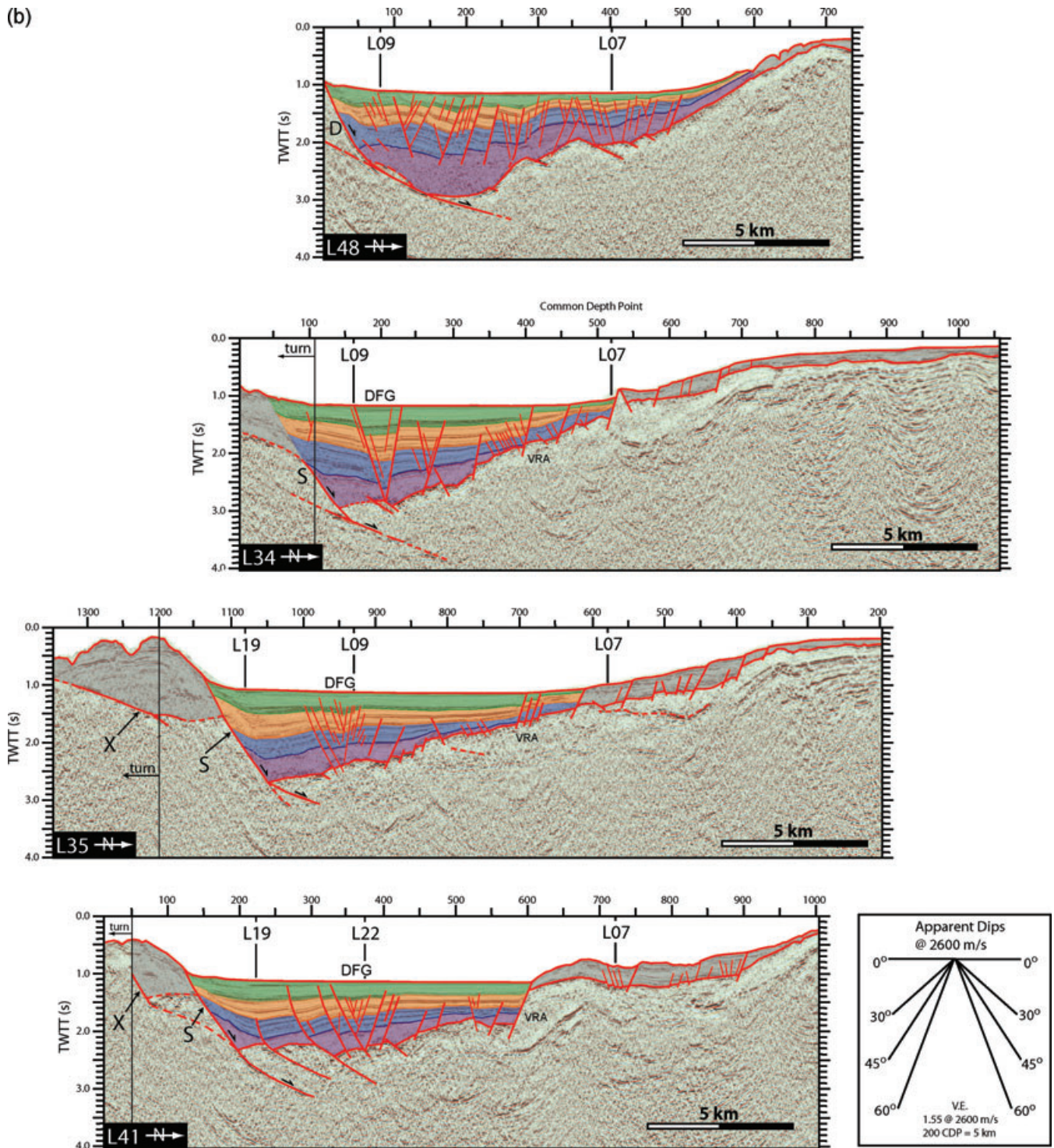


Figure 7. (Continued.)

N–S MCS profile in the western sector, on its eastern side (L27, Fig. 5), though the shallow structure is well imaged by several high-resolution seismic profiles as far west as Aigion (Fig. 3; e.g. McNeil *et al.* 2005; Bell *et al.* 2008, 2009). In the region from Helike to Akrata (Fig. 3), the GoC is bordered along the southern coastline by the N-dipping Helike fault (Fig. 2), which contains large Gilbert fan-deltas on its hanging wall (Rohais *et al.* 2007) and creates significant footwall topography (Fig. 3). The Helike fault is the northernmost of a series of overlapping high-angle (45–50°)

normal faults (Fig. 2; Ori 1989; Sorel 2000; Ford *et al.* 2008; Rohais *et al.* 2008) that formerly extended the northern Peloponnese but are currently inactive at the resolution of GPS (Avallone *et al.* 2004).

Our westernmost line shows no indication of primary structural control by the Helike fault to the south. Instead, the basement and syn-rift horizons imaged in L27 are tilted to the north into a 50° S-dipping fault that controls the position of an axial submarine channel (Figs 5 and 10). Bell *et al.* (2008, 2009) refer to this fault as the

(a)

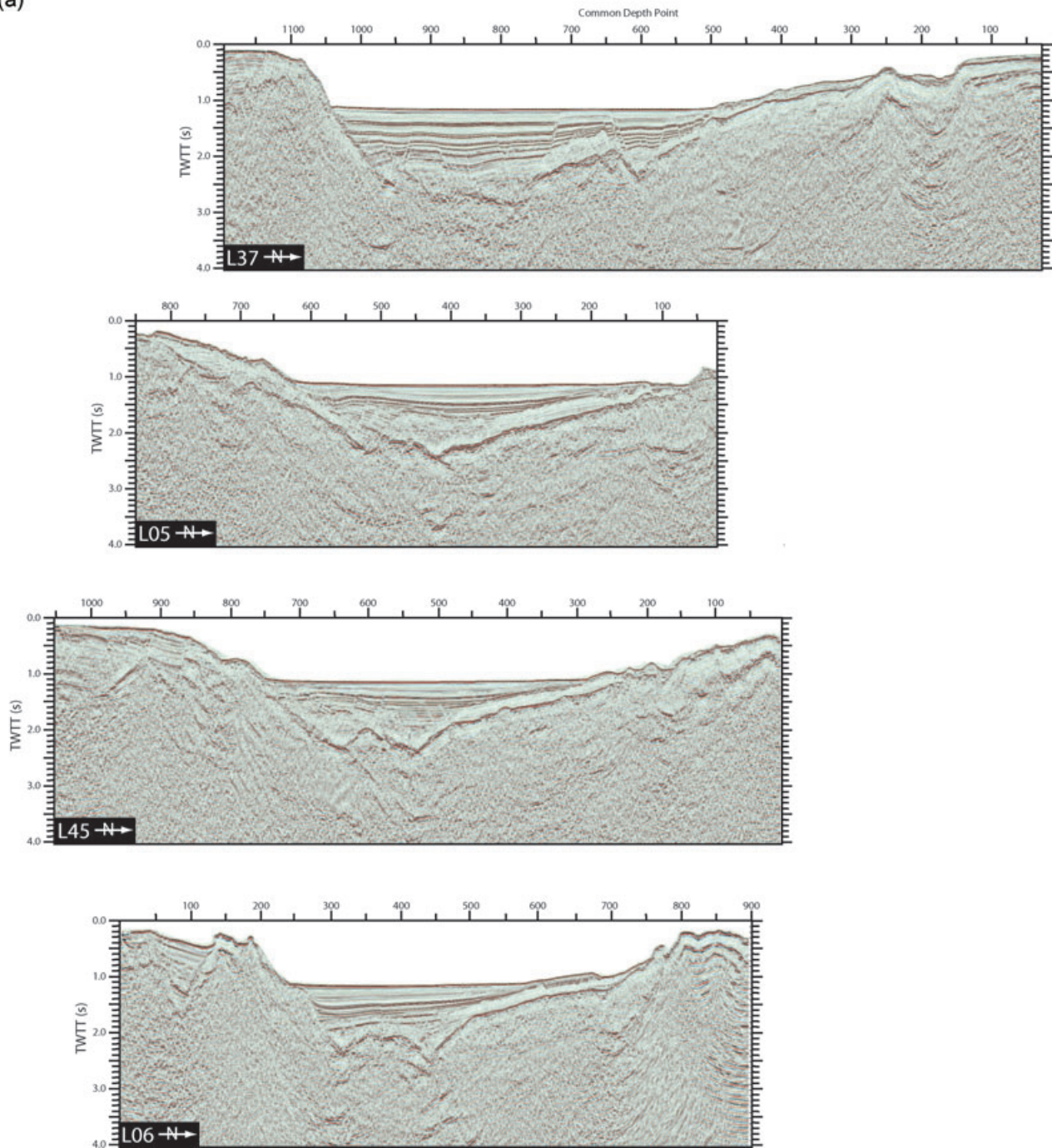


Figure 8. Representative (a) uninterpreted and (b) interpreted EW0108 MCS data from the eastern (L37) and easternmost (L05, L45 and L06) sectors. X, Xylocastro fault; K, Kiato fault; L, Loutraki fault; P, Perahora fault; Per., Perahora Peninsula; VRA, Vrachonisida fault; E, eastern sector; EM, easternmost sector.

West Channel fault (WCF) and their multibeam and high-resolution MCS data reveal the WCF is ~ 12 km in length and extends well beyond the western extent of the EW0108 MCS dataset as a major seafloor fault (Fig. 2). Note that despite clear evidence for the prominence of the WCF it has no strong intrabasement reflector (Fig. 5).

The synrift section thins substantially northwards across the WCF. We identify the late-rift section north of the WCF but correlation around our grid of data, including E–W strike lines (not shown), indicates the early-rift section is not present. This inter-

pretation differs from previous work (McNeil *et al.* 2005; Lykousis *et al.* 2007; Bell *et al.* 2008; Bell *et al.* 2009) that suggested the entire synrift section is present north of the WCF and in the Eratini subsbasin (ESB), north of the horst block imaged in L27 at CDP 470. In our interpretation, subsidence and basin sedimentation widened northwards and were much less asymmetric during the deposition of the 1st late-rift sequence (LRS; *ca.* 680–335 ka, Fig. 4), with offsets on the horst-bounding Eratini Faults (Bell *et al.* 2008) adding to those on the WCF (L27, Figs 5, 10 and 11).

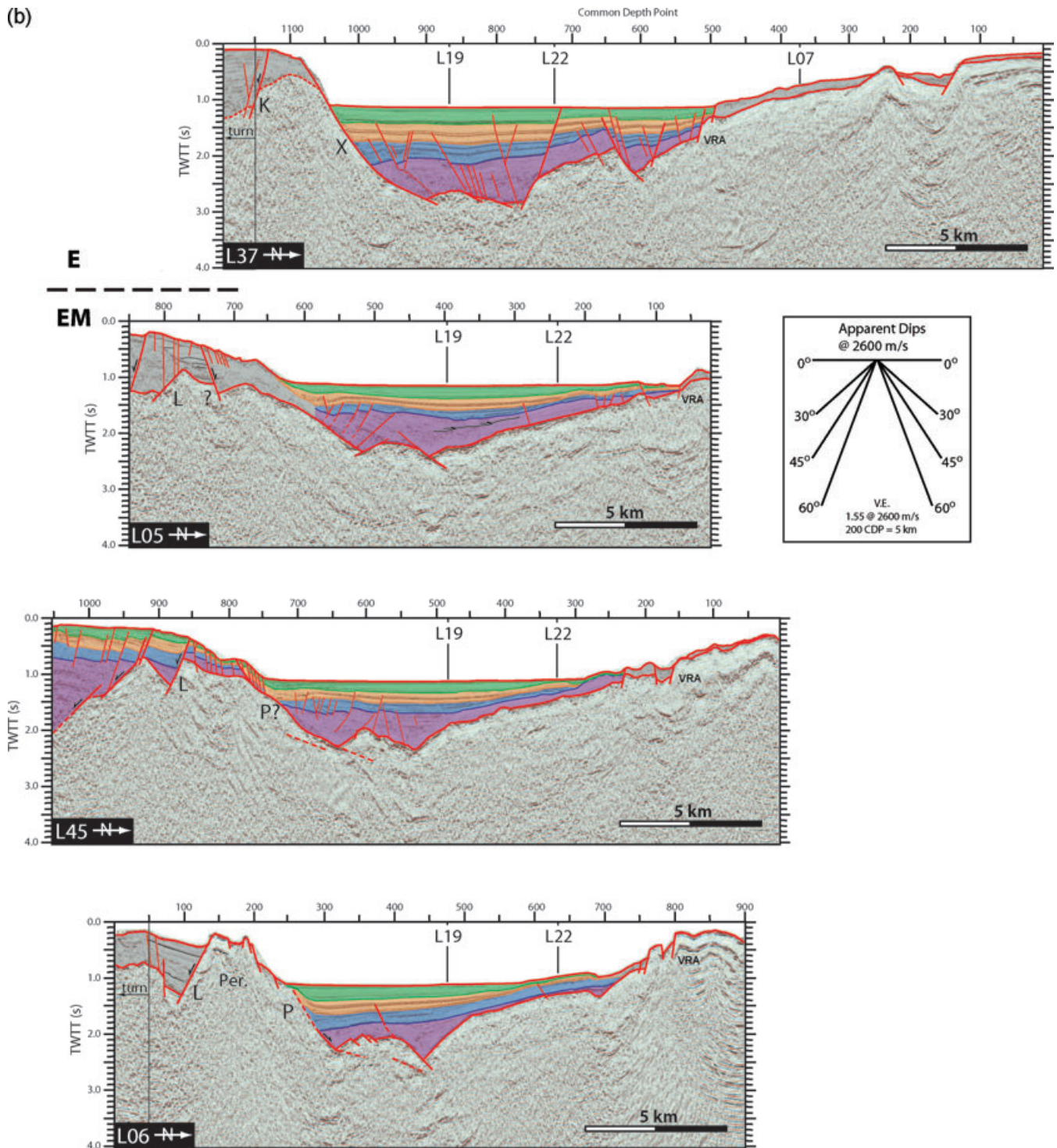


Figure 8. (Continued.)

South of the WCF, an angular unconformity occurs across the boundary between the 1st and 2nd LRS. The 2nd LRS sediment (*ca.* 335–130 ka, Fig. 4) thickens northward into the WCF, but is thin beneath the northern half of the basin and on the northern margin (L27, Fig. 5). As with the underlying sequences (early rift and 1st LRS), the western axial syn-rift section is substantially thinner than the sediments in the central and eastern basin depocentres (see following and Figs 5–8 and 11). We infer that differential subsidence along- and across-axis was present from early in the rift history.

A well-developed system of submarine channels that incise the slope between the western and central Gulf dominate the seafloor morphology adjacent Heliki to Akrata (Fig. 3; McNeil *et al.* 2005). These include the large axial channel that drains eastward from water depths of ~400 m to at least 750 m. The 3rd LRS isopach map reflects the influence of this system on the sedimentation and erosion patterns (Fig. 11). In L27 and L07 (Figs 5 and 9) and adjacent lines (not shown) this pattern of erosion, or channel cut and fill, is not obvious within sequences older than the upper 2nd LRS. We

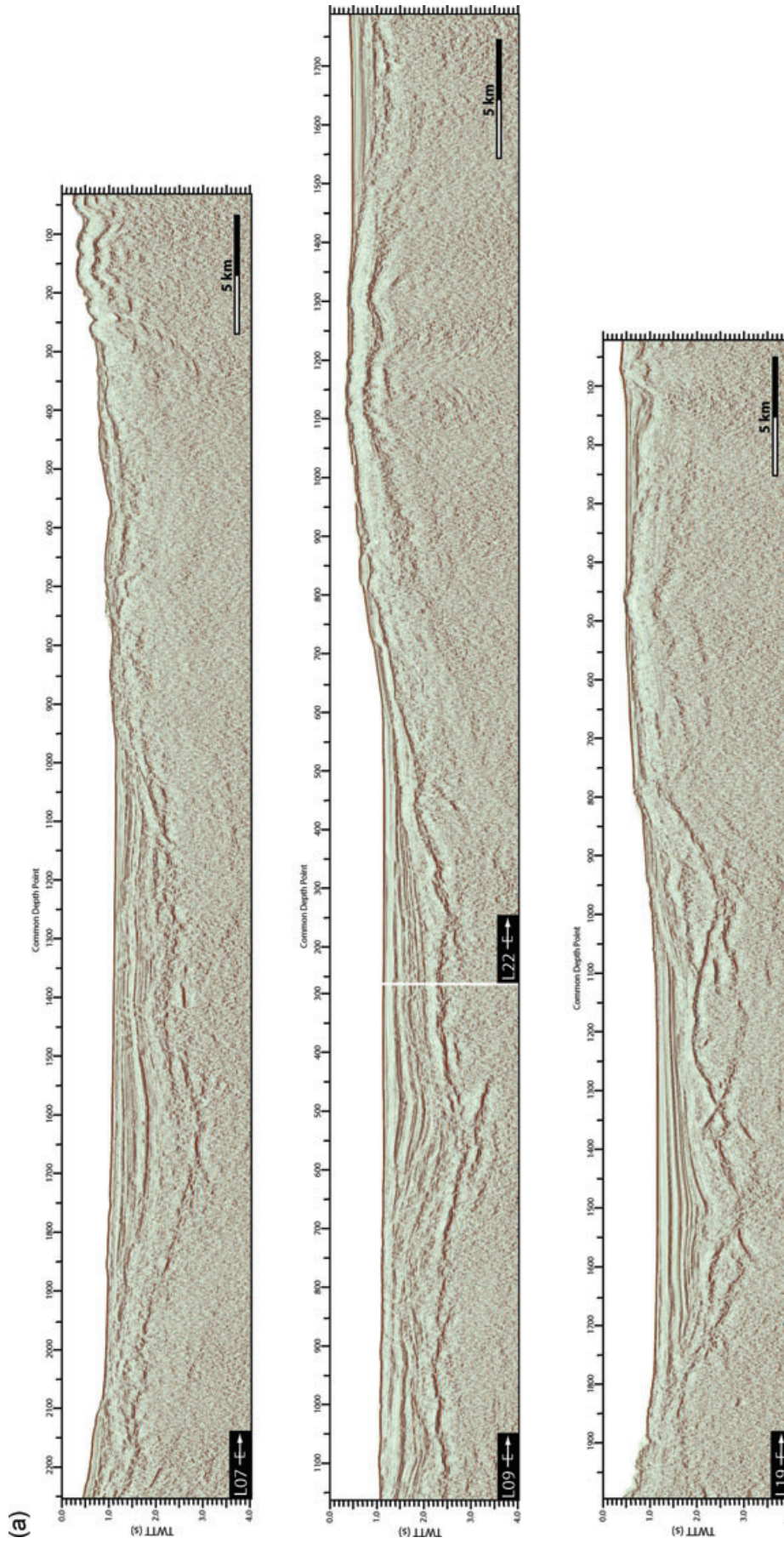


Figure 9. Representative (a) uninterpreted and (b) interpreted E–W oriented EW0108 MCS data. Inferred intrabasement reflectors are heavy red dashed lines and are labelled where they can be confidently correlated with faults imaged in the N–S oriented lines. D, Derveni fault; S, Sithas fault; X, Xylocastro fault.

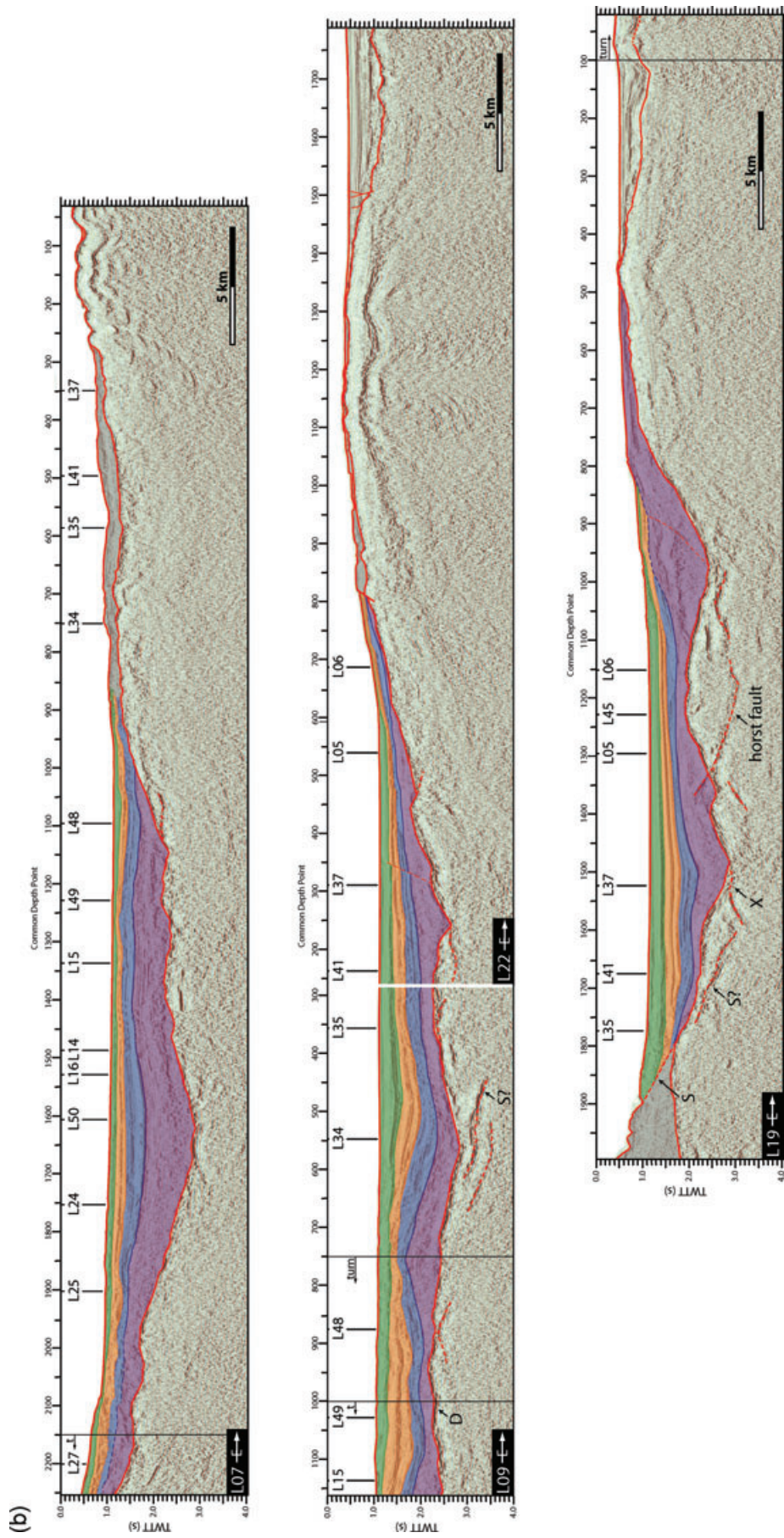


Figure 9. (Continued.)

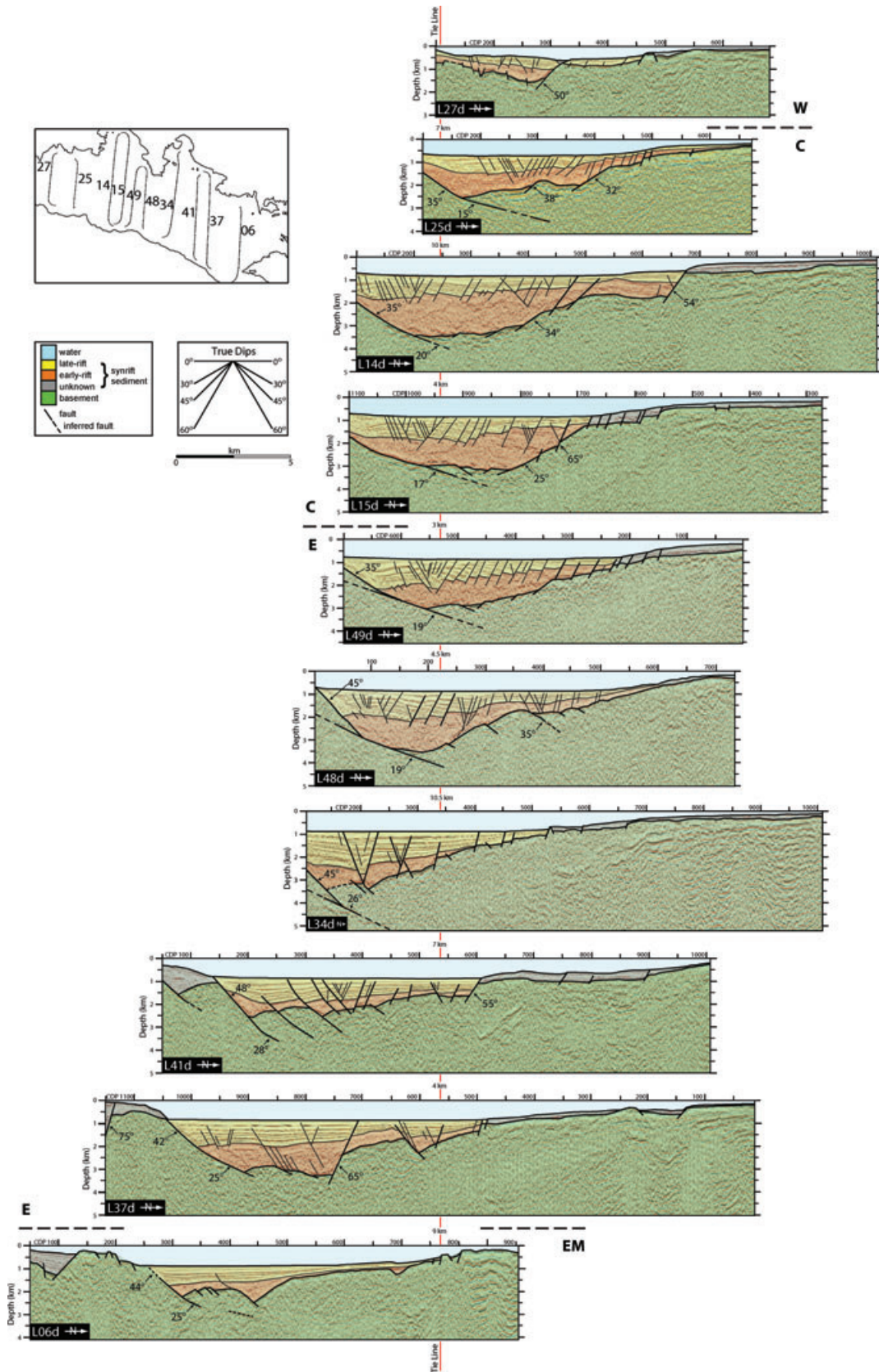


Figure 10. Select post-stack depth converted EW0108 MCS data. Portions of the data collected through turns near the southern margin are not shown. Inset map shows the position of the MCS data. Fault dips are labelled. MCS data are aligned along an ~EW oriented tie line denoted by the red vertical line with distances between the data labelled.

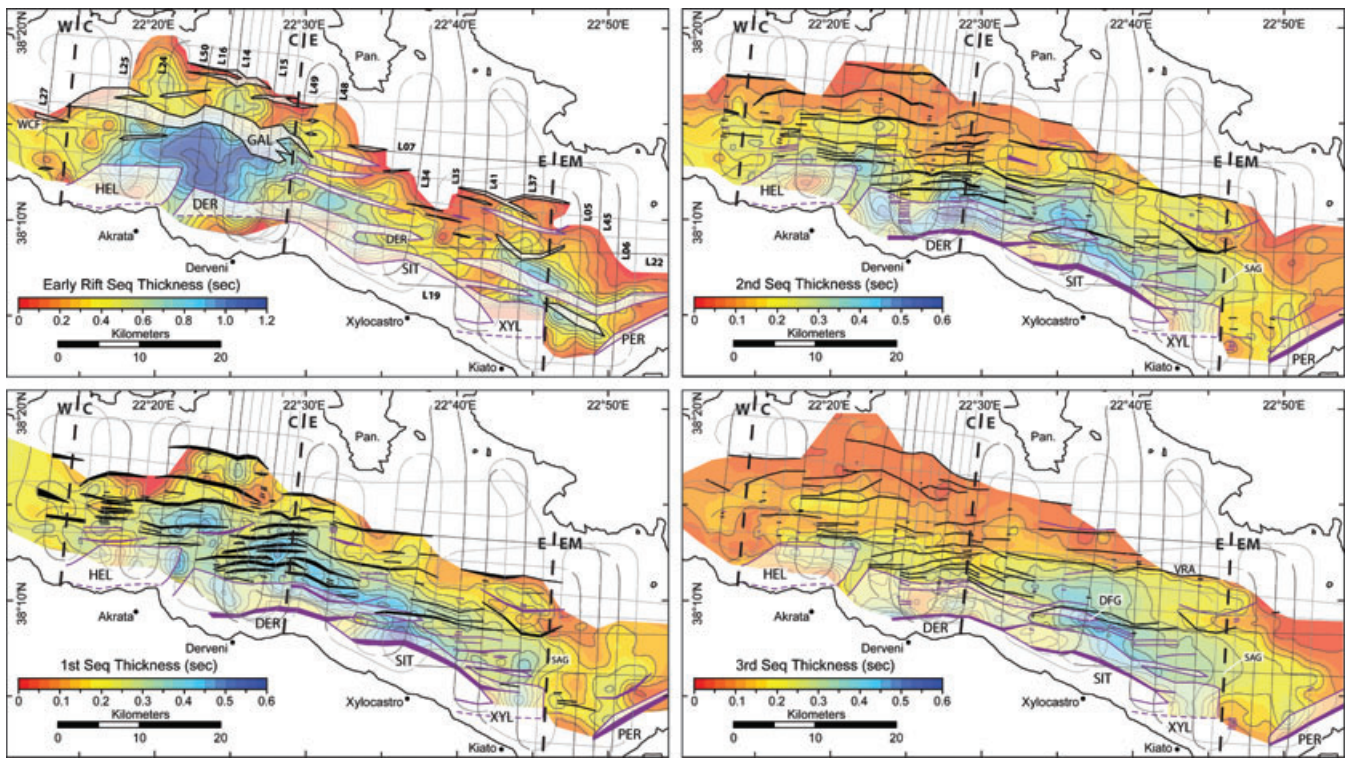


Figure 11. Contoured and colour coded isopach (strictly ‘isochor’) and fault maps for the early-rift section and the three late-rift sections described in the text. Sediment thickness is shown in two-way traveltimes. Note the different colour scales used for the early- and late-rift sequences. North dipping faults are purple and south dipping faults are black. Fault polygon width reflects the amount of offset measured across the fault in that time interval.

infer that the relief between the western and central sectors, and the attendant excision of the axial channel, has increased recently (i.e. since *ca.* 200 ka).

6.2 Central sector

The central GoC rift sector, from just east of Eratini to-and-across the Gulf of Itea, has thick early rift sedimentation in a w- or u-shaped basin controlled in the north by the S-dipping faults south of Galaxidi, and in the south by the N-dipping Helike and Derveni faults (Figs 2 and 11). The dramatic eastward change in the basin architecture of the western versus central rift sectors, apparent from a comparison of L27 and L25 (Fig. 5), occurs over a short distance (the two lines are 7 km apart) that coincides with the eastward deepening Gulf floor (Fig. 3) and basement (L07, Fig. 9), significant crustal thinning (Zelt *et al.* 2005; Sachpazi *et al.* 2007), and proposed basement discontinuities (Papanikolaou & Royden 2007; Ghisetti & Vezzani 2005; Ghisetti & Vezzani 2004). Our MCS strike lines (e.g. L07 in Fig. 9 and L01 in Zelt *et al.* 2004) do not image the proposed basement discontinuities. The Helike and Eratini normal faults are continuous across the sector boundary (Figs 2 and 11). The different geometry of the rift sectors correlates with the different geology of the basement exposed to the north and south of the GoC. Instead of the N–NNW-trending structural fabric of the Pindos nappe in the western sector, the central sector has the Parnassos carbonate platform (whose structural fabric swings to the ESE) to the north, and the basement culmination of the Gavrovo-Tripolitsa nappes, partially covered by rift-related sediments, to the south (Fig. 2).

The Heliki fault becomes a submarine fault where it crosses the boundary between the western and central sectors north of Akrata

(Figs 2 and 3). The Heliki fault polygon also widens significantly across the boundary (Figs 11 and 12). Both L25 and L24 (Fig. 5) approach close enough to the shoreline to image the downdip portion of the Heliki fault, which is offset dextrally from the Derveni fault across a structural ramp (Figs 11 and 12). They reveal a biplanar fault dipping 35° and 15° (L25, Fig. 10), with the hanging wall basement riding on the low-angle segment. Much of the synrift section above the imaged portion of the Heliki fault contains strata that are seaward dipping and nearly fault parallel. An updip (late-rift) transition from dipping strata to landward onlap of the underlying dipping strata occurs in progressively younger sequences towards the eastern tip of the Heliki fault and does not occur past the end of the fault (L25, L24 and L50, Fig. 5). The transition likely reflects a change from direct sediment input across the fault and foreset deposition (prograding submarine fan delta) to indirect sediment input around the eastern end of the fault, from the north and west, resulting in onlap of the dipping strata. Renewed or accelerated late-rift motion on the eastern end of the Heliki fault without significant accompanied motion along the opposed, northern margin faults, would result in southward tilting of their common hanging wall blocks, differential subsidence of the basin, eastward diversion of the Kratis River (north of Akrata, Fig. 3) and the change to along-axis sediment delivery from the submarine channels to the west and north.

The Derveni fault dip is intermediate angle ($\sim 35^\circ$) near the seafloor and extends downdip in a listric to biplanar fashion to a low angle ($17\text{--}20^\circ$) in the basement where it loses definition beneath ~ 4 km depth (L14 and L15, Fig. 10). The data do not approach close enough to the southern shoreline on L50 and L16 (Figs 5 and 6) to image the up dip and presumably steeper portion of the Derveni fault, which underlies the slope to the south and extends westward

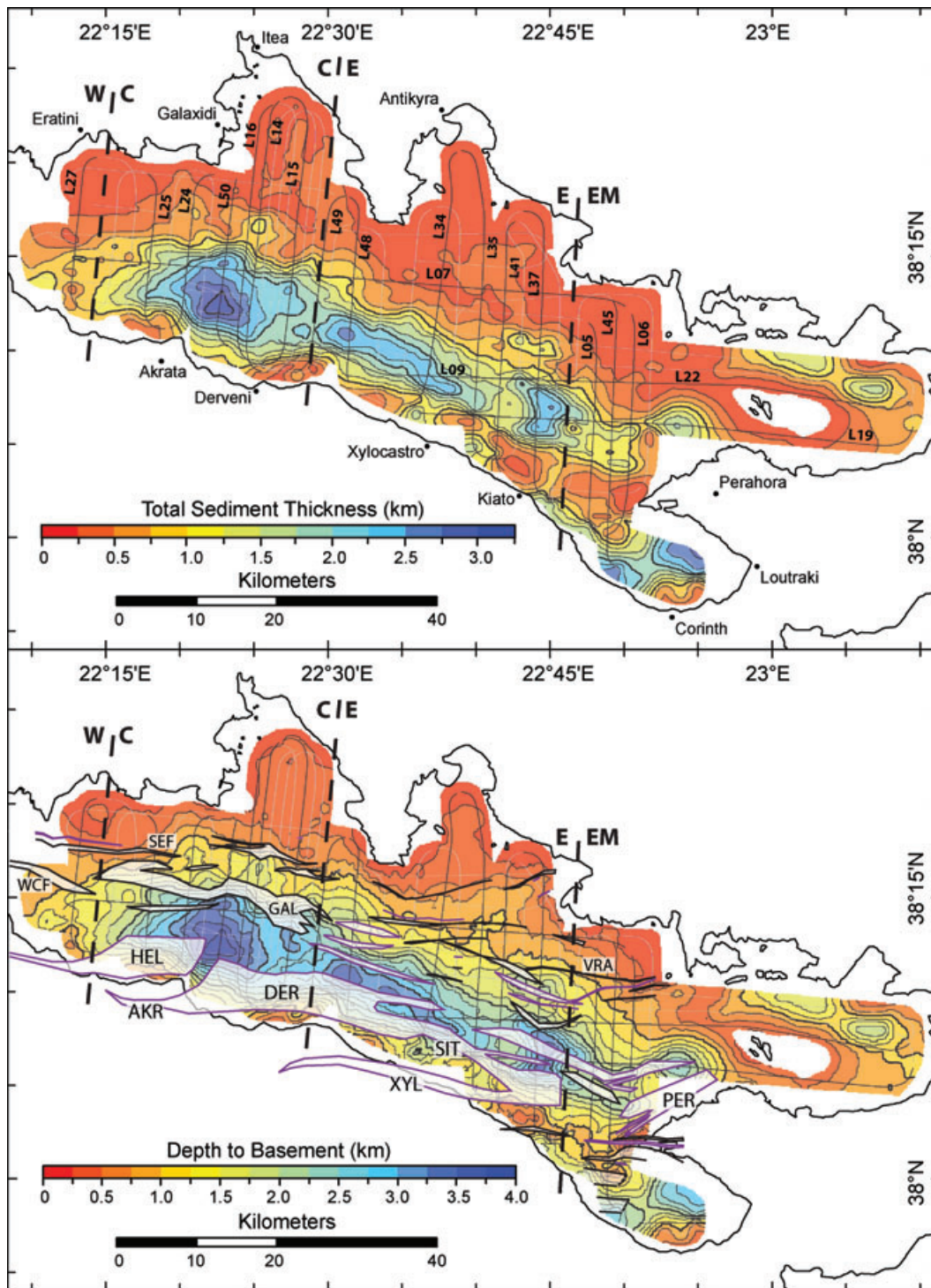


Figure 12. Total sediment thickness map in depth calculated using the linear velocity gradient described in the text (top panel) and total depth to basement map calculated by adding the total sediment thickness to the seafloor bathymetry (bottom panel). Thin contours are every 0.25 km and thick contours are every 1.0 km. Basement fault polygons are overlain on the depth to basement map and discussed in the text. The boundaries of rift sectors discussed in the text are shown as bold dashed lines.

for ~ 10 km as the subaerial Akrata fault (Rohais *et al.* 2007; Fig. 2).

In addition to the Heliki and Derveni faults along the southern margin, the central sector of the basin is controlled by a S-dipping, basement-bounding, northern margin fault, which we term the Galaxidi fault, after the town to the north (Fig. 3). Stratal

thickening and tilting of the early- and late-rift sections into N- and S-dipping normal faults indicate the early and continued activity of an opposed system of border faults in the central sector. The present dip of both sets of early-rift-depocentre-bounding faults is $\leq 35^\circ$ (Fig. 10). They must have cut one or other or both of themselves at depth, in order for their common hanging wall blocks to subside.

The Galaxidi fault does not reach the seafloor and has been replaced by a set of high-angle faults whereas the southern margin faults are active and create significant footwall topography.

Distributed extension in the overlap zone between these faults results in a >2-km-thick sediment section and the deepest GoC basement (Fig. 12). The depocentre was established early and modified by the growth of all three faults (Fig. 11) but the thickest basin-wide sediment and deepest basement occurs on the western end of the submarine portion of the Derveni fault, where it is low-angle (e.g. L50, Fig. 5; L16, Fig. 6; and 17° in L15, Fig. 10). This location is far from the surface outcrop of the fault at the coastline and we do not image the normal drag and local thickening at the base of the slope that characterize shallower portions of the fault to the east (compare L50 and L16 with L49, Figs 5 and 6). Synrift strata in both the early- and late-rift sections gently dip to the north between L24 and L50 (L30, not shown) where a structural ramp occupies the overlap zone between the Heliki and Derveni faults (Fig. 11). We infer the ramp is a long-lived structure that has acted as a pathway for sediment transport and influenced stacking patterns above the adjacent faults.

As shown on L25–L15 (Figs 5 and 6) and in additional MCS data from the same area (Zelt *et al.* 2004), the central sector early-rift depocentre has controlling border faults to both the north (Galaxidi) and south (Helike and Derveni). Only in the vicinity of L15 does northward basement dip and stratal tilting and thickening into the Galaxidi fault (Figs 6, 10, 11) support the interpretation based on one industry MCS line from the same region that the early-rift GoC central basin structure is that of an asymmetric graben tilted to the north (Moretti *et al.* 2003; Sachpazi *et al.* 2003; Bell *et al.* 2009). This contrasts with the south-tilted asymmetry evidenced on L25 and L16 and the more typical quasi-symmetry of the thickest early rift section seen on L24, L50 and L14 (Figs 5 and 6). The EW0108 data show that, within the central sector, faults along both margins were active throughout rifting and that the early rift dominance of the Galaxidi fault in the east near L15 was the exception (Figs 10 and 11).

The late-rift section across the central sector more often thickens to the south and/or into local depocentres across sedimentary faults not clearly linked to basement structures. From this observation, together with the significant footwall topography of the southern margin faults in the central sector (Fig. 3), and the lack of the same for the south-dipping, northern margin faults, we infer that Heliki-Derveni-Akrata became the fault system accommodating the majority of extension.

The transition occurred during 1st LRS deposition when localized depocentres were present mid basin (near the intersections of L07 on L24, L50 and L16 and near CDP 850 on L15), near the eastern tip of the Helike Fault (Fig. 11), above the Derveni Fault, and against the northern margin on L16 and L14 (Figs 5, 6). In addition, 1st LRS sediments thicken and lap onto the early rift sequence above the Galaxidi fault, where a number of high-angle faults create elongate, late-rift depocentres (L25 and L24, Figs 5 and 11). These late-rift faults often lose clear expression in the thick early rift section but penetrate into basement on the northern margin, variably offsetting or soling into the lower-angle portion of the Galaxidi fault. Except for the southern border faults, the late-rift faults in the central sector are (nearly) all high angle. The lack of a clear connection between these faults and the basement suggests significant early-rift fault rotation and formation of a new generation of high-angle faults at the early- to late-rift transition (*ca.* 680 ka). In contrast, much of the mouth to the Gulf of Itea is cut to basement by a high-angle, south-dipping normal fault system that has been active from early

rift times to the present (e.g. north of L02 on L50, L16 and L14, Figs 5 and 6).

Across most of the central sector, relative stratal thicknesses show the southern margin dominance beginning within the 2nd LRS (Figs 5, 6 and 11). A 2nd LRS depocentre is present adjacent to the central section of the Derveni Fault (e.g. L50–L49, Figs 6 and 11), localized depocentres have migrated southwards, and the 2nd LRS sediment is thickest on the southern side of mid-basin on L25 and L24 (Fig. 5). Slope-parallel deposition of sediments on the eastern Heliki fault continued into the 2nd LRS, whereas sediment onlap occurs thereafter and on the northern margin throughout. In general, the onlap onto both the northern and southern margins reveals that late-rift depocentre subsidence has outpaced sedimentation.

Near the beginning of the 3rd LRS (*ca.* 130 ka), a rollover anticline formed above where the hanging wall basement pulled off from the intermediate- onto the low-angle portion of the Derveni Fault and the crest of the anticline collapsed, forming nested grabens bounded by high-angle faults (L16–L15, Fig. 6). Sachpazi *et al.* (2003) infer that the breakaway was accompanied by a significant increase in extension rate. Strata exhibit normal drag and the 3rd LRS is locally thick on the hanging wall of the submarine portion of the Derveni fault but the late rift pattern of localized depocentres reflects broad subsidence, not only associated with the border faults but also with extension below the deep basin. The extension and subsidence within the central GoC sector sediments are accommodated on numerous E–W and WNW-trending, north- and south-dipping, high-angle faults that offset the late rift section (Figs 5 and 6).

6.3 Eastern sector

The transition between significant early-rift structural control along the northern margin in the central sector and the long-lived dominance of southern margin faults in the eastern sector occurs over a very short distance. The eastern tip of the Galaxidi fault controls a large early-rift depocentre in L15 but a few kilometres to the east the fault splits into smaller segments and basement offset becomes distributed and decreases in L49 (Fig. 6). By L48 the basement and the entire synrift section are tilted to the south and the early-rift depocentre is near the Derveni fault (Figs 7 and 11). North of the depocentre, shallow-angle (<30°), north-dipping normal faults create a series of small basement blocks. Major changes in early-rift thickness do not occur across these faults, indicating they were abandoned prior to significant deposition. The lack of a large northern margin fault keeps these basement fault blocks shallow and consequently they may be better imaged than to the west, where we infer their presence in the mid-basin.

On the northern margin, the change is from the little-faulted Gulf of Itea (see northern ends of L16, L14 and L15, Fig. 6) to the normal faults with significant relief crossing the Pangalos Peninsula (Figs 2 and 3). On the southern margin, the transition is marked by a decrease in distributed normal faulting south of the Gulf (Fig. 2). The southern border faults in the eastern sector include the Derveni, Sithas and Xylocastro faults, which exhibit major overlap (Figs 2 and 12). The basement offset of these faults is linked at depth (Figs 11 and 12), an observation that is not apparent from their surface fault traces (Fig. 2).

The Derveni fault, and associated 3rd LRS rollover anticline with crestal graben, crosses the central-eastern sector boundary. The fault exhibits a biplanar geometry, with low-angle basal dip (19°) and an updip portion that steepens from 35° in L49 to 45° in L48 (Figs 6, 7 and 10). A high-angle splay from the Derveni

fault extends eastwards into the basin where it forms the southern boundary of the EW-trending Derveni fault graben (DFG, L34, L35 and L41, Fig. 7). Synrift strata in both the early- and late-rift sections gently dip towards the DFG in L34 and an adjacent line to the west (not shown). The high-angle DFG-bounding faults in the sedimentary section connect to the shallow-angle, north-dipping faults in the basement (e.g. L34, Fig. 7).

South of the Antikyra Gulf (Fig. 3), we identify a major N-dipping, basement bounding, southern margin fault between the Derveni and Xylocastro faults. Following our previous work (e.g. Weiss 2004), we term this structure the Sithas fault, after the Sithas River, which crosses the coastal plain just east of Xylocastro and has deposited a submarine fan at the base of the slope on the fault hanging wall (Figs 2 and 3). Bell *et al.* (2009) refer to this structure as the Likoporia fault. As opposed to the Heliki, Derveni, and Xylocastro (see following) faults with both onshore and offshore portions, the Sithas fault is strictly submarine. It dips 45–48° near the seafloor and intersects a shallow-angle (~26°) reflector (L34), possibly cuts a shallow-angle reflector (L35), or is listric-to-biplanar decreasing from 48° bounding the sediments to ~28° in the basement (L41; Figs 7 and 10). In L34, the downdip portion of the shallow-angle reflector is imaged discontinuously to a depth of ~5 km and it extends up dip to the south beneath the Sithas fault a short distance. The turn near CDP 100 in L34 causes the Sithas fault to appear to ‘roll over’ rather than intersect the seafloor. The hanging wall basement meets the Sithas fault footwall above the biplanar intersection in L34. Where the basement hanging wall has not pulled off from the higher- to shallow-angle part of the Sithas fault but instead has extended on synthetic shallow-angle faults, the DFG formed early in the 3rd LRS (e.g. L34, L35, L41, Fig. 7). This, together with the thin early-rift sequence, contrasts with the central sector geometry, and hence no rollover and crestal collapse graben structure has formed here.

The EW0108 data help to constrain the continuity, geometry and location of the Xylocastro fault, which is clearly imaged as a major offshore border fault (L37, Fig. 8) separate from the shoreline parallel Sithas fault (L35 and L41, Fig. 7). It approaches the coast, creates a basement block with a thick synrift section south of the Sithas fault (see following), and extends onshore for >20 km to the west. Our subaerial extension of the Xylocastro fault (Fig. 2) is partially based on recent geologic mapping (Place *et al.* 2007), that shows the Xylocastro fault directly along strike from and adjacent to the submarine portion of the fault. Although footwall topography dies out rapidly as the fault approaches the coastline, no major N–S oriented transfer structures such as those suggested by Place *et al.* (2007), are observed north of where the fault crosses the shoreline (see E–W trending lines L09 and L19, Fig. 9). Calcite from the Xylocastro fault hanging wall indicates the subaerial portion of the fault was active at 1 Ma and 108 ka (Causse *et al.* 2004) and studies have suggested the subaerial portion of the fault is locked (Flotte *et al.* 2001).

The downdip portion of the Xylocastro fault is imaged south of the Sithas fault in L35 and L41, and may form the southern low-angle fault in the basement on L34 (Fig. 7). The updip portion of the Xylocastro fault in L37 has one of the clearest southern border fault reflectors imaged in the EW0108 dataset (Fig. 8). Its dip decreases in a listric fashion from ~45° at the seafloor to 20° near the base of the synrift section (Fig. 10). The majority of late-rift strata terminate against the fault footwall without exhibiting normal drag and only the 1st late-rift sequence exhibits a small amount of reverse drag (Fig. 8). Unlike on the immediately adjacent lines (not shown) and elsewhere in the GoC, the basin fill imaged in L37

does not interfinger or merge with slope parallel strata against the southern margin. The early-rift section is substantially thicker adjacent to the Xylocastro fault past the eastern end of the Sithas fault (Fig. 11).

Stacking velocities support the interpretation that a thick (~1 km) sediment section sits on top of the tilted block between the Xylocastro and Sithas faults (Fig. 7). The sediments on top of the fault block are probably temporally equivalent to the early-rift section and they are incised by the offshore extensions of the river system between Xylocastro and Kiato (Fig. 3), as seen near the turn on L35. We infer that early-rift extension and deposition was distributed across the overlapping portions of these faults and subsequently shifted northward towards the Sithas fault and Derveni fault splay during late-rift deposition (Fig. 11) while the offshore portion of the Xylocastro fault remained active. This is similar to the structural and stratigraphic evolution near the eastern tip of the Heliki fault, where the Akrata-Derveni-Heliki faults overlap in the central sector, and supports suggestions that extension across the onshore portion of the Xylocastro fault progressively has been shifted to the submarine Sithas fault during late-rift sequence deposition (Bell *et al.* 2009). Consequently, the early-rift sequence likely extends over a much broader region than what we show in Fig. 11. A more complete isopach map would stretch southward to at least the subaerial portions of the Xylocastro and Akrata-Derveni faults, eastward into the Alkyonides Gulf, and into the Gulf of Lechaio, as well as onto the northern margin where we are unable to reliably differentiate the multiple rift sequences within the thin sediments (Figs 7 and 8). Westward, the early-rift isopach would also extend to Aigion on the hanging wall of the inactive Pirgaki-Mamousia fault (Ghisetti & Vezzani 2004; Ghisetti & Vezzani 2005; Backert *et al.* 2010).

Across much of the eastern sector, and adjacent to the Sithas fault in particular, the early-rift sequence is thin, with localized thickening across some of the basement fault blocks (e.g. L34, L35 and L41, Fig. 7). The northern extent of early-rift deposition is narrow, particularly on L34 and L35 where the early-rift sediments lap onto and pinch out against the southward-tilted basement. The early-rift isopach map reveals that the eastern sector, from east of L48 to west of L37, was structurally higher than the adjacent early-rift depocentres (Fig. 11). This structural high subsequently subsided, as evidenced by its late-rift section being substantially thicker than the early-rift section. Faults along the northern margin are much smaller than the southern border faults, forming half-graben or asymmetric graben geometries (e.g. L48–L35, Fig. 7). Further, the basin fill across the eastern sector does not record a complex early-rift history and most faults maintain a high-angle through the early-rift section and intersect or offset the basement. These include the mid-basin horst block faults north of the Xylocastro fault (e.g. L37, Fig. 8), which are high angle (55–65°) and planar, and the multiple small, S-dipping, northern margin seafloor faults (L34–L37, Figs 7 and 8). Synthetic, shallow-angle basement faults occur in the mid-basin, between the Sithas fault and the DFG; they extend updip in a listric fashion and are high angle in the sediment section (e.g. L41, Fig. 7).

The 2nd LRS depocentre is in the south above the Derveni fault (e.g. L16–L49, Fig. 6) and in the mid-basin on L48–L34 (Fig. 7). This pattern is repeated eastwards: south against and above the Sithas fault on L35 then trending east into mid-basin on L41–L45 (Figs 7, 8 and 11). The 2nd LRS sediment exhibits normal drag against the southern border faults, sometimes thickening against the faults (e.g. L35) but more often thinning onto the underlying sequence where the depocentre shifts away from the border fault, commonly above synthetic low-angle basement faults (e.g. L41, Fig. 7). Another example of the latter are the thick 1st and 2nd LRS

above the north-dipping fault that reaches half way through the 2nd LRS at CDP 850–890 in L37 (Fig. 8).

During deposition of the 3rd LRS there is an almost symmetric subsidence of the eastern sector about a 095°-trending axis (Fig. 11). Together with sedimentation keeping the seafloor nearly flat, this requires similar net subsidence on the northern as southern fault systems. Furthermore, on L37 (Fig. 8) the 2nd and 3rd late-rift sequences are equally thick across the basin between CDPs 730 and 1000. Their lack of tilting requires that the bounding low-angle Xylocastro fault and high-angle horst fault cross-cut one another at depth. The maximum 3rd LRS thickness occurs in the narrow axial graben: the DFG which formed early in the 3rd LRS. The conformity of 1st and 2nd LRS isopach thicknesses across the DFG shows that the graben was not present at those earlier times (e.g. L34, Fig. 7). The distinct E-W trend of the 200 and 150 ms LRS isopach contours indicate the northern margin faults in the eastern sector have lengthened by linking at least three separate 2nd LRS fault segments. The long and sinuous north and south dipping faults that localize the DFG formed during the 3rd LRS.

Near the southern end of L37 (Fig. 8) and L42 (not shown), there is a high-angle (75°) south-dipping normal fault with a >1-km-thick sedimentary sequence to the south of the Xylocastro fault. We refer to this as the Kiato fault (K, Fig. 8) (after the nearby town) and propose that it may be the offshore continuation of a similar fault inferred to bound the south side of the Xylocastro horst (KIA, Fig. 2; Sakellariou *et al.* 2004).

6.4 Easternmost (Perahora-Lechaio-Alkyonides) sector

The easternmost sector comprises the portion of the rift that includes the Perahora Peninsula and the Alkyonides and Lechaio subbasins (Figs 2 and 3). The boundary on the western side of the sector coincides with the transition from the Parnassos to the Pelagonian nappes and a change in the dominant strike of major faults. Some of the Perahora Peninsula surface faults were activated during the 1981 earthquakes (Jackson *et al.* 1982; Leeder *et al.* 2005; Fig. 2). Seafloor faults in the main basin are restricted to the Gulf margins and rarely offset the seafloor at depths >800 m (Figs 2 and 8). Major N-dipping, southern margin faults do not cross the sector boundary and the transition from a steep sediment-basement contact across the Xylocastro fault in L37 to a shallow dipping top of the basement and conformable overlying strata (e.g. between CDP 520 and 650 on L05, Fig. 8) indicates no major southern border fault, but rather a slightly more tilted mirror image to the northern half of the basin (i.e. a dip slope tilted north into the south-dipping fault bounding the horst between CDP 450 and 500).

From west to east L05, L45 and L06 (Fig. 8) image a portion of the NE-trending Perahora fault and E–W-trending faults to its south. The portion of the Perahora fault imaged in L06 decreases apparent dip from ~44° near the seafloor to ~25° in the basement (Fig. 10). Those values correspond to real dips of 54° and 33°, respectively given the ~45° direction angle between the N–S MCS line and the NW dip direction. The continuity of the Perahora fault to the west across the mouth of the Gulf of Lechaio (GL in Fig. 3) is uncertain. We terminate it on L45, where the basement is steep and there is 2nd and 3rd LRS thickening towards the southern margin (Fig. 8), suggesting that it is a fault (probably the westward end of the Perahora fault, Figs 2 and 8).

As seen on the Perahora Peninsula, which is bounded by the NW-dipping Perahora fault and the south-dipping Loutraki fault (LOU in Fig. 2), there are several normal faults of alternating north- and

south-dip that cut the basement high that crosses the mouth of the Gulf of Lechaio (Fig. 8). We correlate the intense faulting imaged in L45 between CDP 750 and 850 with east-trending faults that cut the tip of the Perahora Peninsula but it may be associated with splays of the Perahora fault. L06 images the submerged Perahora Peninsula horst block and the thick sediment section (>2 km) in the Gulf of Lechaio subbasin to the south (Figs 8 and 12). L05 and L45 also image the horst block and subbasin and L45 shows our jump correlation of GoC seismic sequences into the latter. In addition to the Loutraki fault seen on L45 and L06, there is another south-dipping fault further south on L05 and L45 (Fig. 8). Additional, single channel, seismic data (Perissoratis *et al.* 1986; Sakellariou *et al.* 2004) as well as L43 and L44 (not shown) confirm northward stratal dips in the Lechaio subbasin sediments.

Both the Perahora fault and faults bounding the horst to the north affected early-rift sedimentation (Fig. 11). On L45, L05 and L38 (not shown) stratal thickening of the early-rift section is towards a central basement horst block bounded by opposed low-angle normal faults, forming a double-swing-door geometry. North of the horst, and south of small-throw high-angle faults along the northern margin, the basement and its mostly conformable early-rift section are tilted south to the basin centre, then successively unclipped by the late-rift section. On L06 (and especially on L39 to the east, not shown), the early-rift section is thickest on the hanging wall of the northern horst fault and early-rift strata terminate against the fault suggesting it was dominant in this part of the basin during early-rift deposition. At CDP 445 in L06 the northern limb fault accommodated more basement subsidence during early rifting than the Perahora fault. It extends to the west and also affected early-rift deposition in the eastern sector although its strike changes across the sector boundary (Figs 11 and 12). The southern horst-bounding fault (L05 and L45, Fig. 8) occupies the gap between the Xylocastro and Perahora faults (Fig. 11). Early-rift strata dip towards the horst. Associated high-angle faults were active into the 2nd LRS (Figs 8 and 11).

Although not included in the isopach map, a thick early-rift section imaged north of the eastern tip of the Perahora fault (e.g. L19 at CDP 950, Fig. 9) can be seen in the total sediment thickness map (Fig. 12). The depocentre is not well covered by the MCS data although it is probably related to the central-eastern limb of the Perahora fault based on the position of L19 relative to the surface fault trace (Figs 2 and 3). The depocentre is significantly thicker than the early-rift section imaged on the hanging wall of the western end of the Perahora fault in L06 (Fig. 8). Slip along the Perahora fault progressively outpaced slip along the fault to its north during late-rift sedimentation. In L06 the early-rift section above the basement horst is thinner than on the lines to the west. The synrift section thickens and is tilted to the south, forming a half graben against the Perahora fault against which late-rift sequences exhibiting normal drag (Fig. 8).

North of the Gulf of Lechaio, between the Xylocastro and Perahora faults, the thickest late-rift horizons and a local depocentre are developed in a mid-basin sag near the intersection of L19 with L05 and L45 not associated with the major faults along either margin (Figs 8 and 12). Space accommodation, therefore, must be related to extension in the basement and not with faults imaged at the seafloor. The northern limb of the early-rift horst block and an associated intrabasement reflector occur in this location near the intersection of L05 and L45 with L19 (Fig. 9).

A basement high separates the main basin from the Alkyonides Gulf subbasin to the east (Fig. 2; L22 and L19 in Fig. 9). Synrift sediments thin rapidly eastward approaching the structural high off

which the late-rift section in particular thickens westward, towards the portion of the Gulf controlled by the large southern margin faults.

The relatively shallow (<400 m) Alkyonides Gulf is bounded by high-angle faults along both margins and high-resolution seismic surveys reveal the presence of alternating basin-fill sequences that have also been correlated to sea level cycles (Collier *et al.* 2000; Leeder *et al.* 2005; Sakellariou *et al.* 2007; Bell *et al.* 2009). However, the distinct alternating sequences recognized in the main GoC basin (Fig. 4) are not similarly imaged by the EW0108 data in the Alkyonides Gulf. Rather, the data image >1 km of sediment composed of an upper, highly reflective sequence with conformable strata sitting above a lower sequence with strata that onlap basement topography (e.g. CDP1500–1700 in L09, Fig. 9). Although the timing is debated, we suspect that the sequence boundary relates to a proposed shift from symmetric to asymmetric subsidence and strain localization along the southern coastal fault system possibly at the early/late-rift boundary resulting in a southward thickening upper sequence (Leeder *et al.* 2005; Sakellariou *et al.* 2007; Bell *et al.* 2009). Leeder *et al.* (2008) suggest that Megara Basin abandonment and development of the Alkyonides Gulf border faults occurred when the Corinth Rift formed (in their view, at ca. 2.2 Ma).

7 TOTAL SEDIMENT THICKNESS AND DEPTH TO BASEMENT

The EW0108 MCS dataset is the first to provide images that enable a time progressive view of the entire faulting and sedimentation history of the central and eastern GoC from the top of the basement to the seafloor. The depth-converted total sediment thickness map derived from our dataset (Fig. 12) has been added to the seafloor bathymetry (Fig. 3) to create a total depth to basement map (Fig. 12) to better understand where and how accommodation space has been created through time. The sediment thickness time to depth conversion was performed using seafloor and basement horizon picks for the MCS data and the linear velocity gradient described in Section 4 of this paper.

Seafloor depth (Fig. 3) is a reasonable guide to sedimentary thicknesses (Fig. 12) with some notable exceptions. The modern sedimentary depocentre, at water depths exceeding 700 m, overlies the region of thickest sediment accumulation, which parallels the southern coastline. Within this ESE-elongate region, there are three local sediment thickness maxima (>2 km), of which the westernmost is the thickest (>3 km). Contrary to previous suggestions (Armijo *et al.* 1996; Moretti *et al.* 2003), the thickest sediment accumulation in the Gulf is not located beneath where the seafloor is the deepest (~890 m, in the southeast of the basin).

The depocentres do not hug the southern shoreline, as might be expected in a simple half graben controlled by a steeply dipping fault along that margin. The location of the thickest sediment section and deepest basement imaged in nearly all of the EW0108 MCS data is above where the top of the hanging wall basement intersects the southern border fault system, whose dips typically decrease with depth. Therefore the thickest sediment accumulations are located seaward from where the border faults intersect the seafloor, being offset to the north of the southern GoC margin by as much as 10 km. This is further modified by the presence of variably developed faults such as the northern margin faults, that widen the total thickness depocentre in the west, and the horst block faults (L37), that irregularly shape the depocentre in the east. South of the 1-km-thick

contour the total sediment thickness decreases abruptly as horizons terminate, exhibit normal drag, or interfinger with slope parallel strata against the southern border faults.

The subsidiary basins along the northern Gulf margin beneath the Gulfs of Itea and Antikyra contain <0.5 km of sediment whereas both the Alkyonides Gulf and the Gulf of Lechaio, at the eastern and southern Gulf margins, respectively, contain fault-bounded basins (Fig. 2) with >1 and >2 km of sediment, respectively (Fig. 11a). The fault polygons overlain on the depth to basement map show our interpretation of the basement-basement fault offsets from the full EW0108 MCS grid of data (Fig. 12). The wider fault polygons reflect the low- to intermediate-angle dip of large-offset faults. The updip and/or onshore portions of the Heliki, Akrata-Derveni, and Xylocastro faults match the surface fault traces shown in Fig. 2 and were determined from some of the most recent published fault maps (e.g. McNeil *et al.* 2005; Place *et al.* 2007; Rohais *et al.* 2007; Rohais *et al.* 2008; Palyvos *et al.* 2010) and from examining the regional topography (Fig. 3). Not surprisingly, the few very large faults that accommodate significant basement extension are associated with the deepest basement and thickest sediments.

The southern border faults overlap significantly and the basement offset of the Akrata-Derveni-Sithas-Xylocastro fault is linked at depth (Fig. 12), an observation that is not apparent from their surface fault traces (Fig. 2). Even the Xylocastro and Perahora faults are overlapped by the synthetic basement fault in their hanging wall. The thickest sediment in the Gulf occurs in the overlap zones between major border faults and typically towards the ends of individual southern border faults. Localized depocentres associated with north- and south-dipping basement faults are also present but are no longer active or accommodate extension in the basement without accompanying shallow faulting.

The Gulf of Lechaio overlies an asymmetric graben or half-graben tilted to the north against the bounding Loutraki Fault (Fig. 2). The south-dipping faults and thick, north-dipping, sediment section that characterize the Lechaio subbasin contradict the thick-elastic plate model of rift-flank uplift (Armijo *et al.* 1996) proposed to explain the flight of marine terraces exposed on the Corinthian plain to the south (Keraudren & Sorel 1987; Armijo *et al.* 1996). These terraces do not simply lie on the footwall of the Xylocastro fault and are not formed solely by rift flank uplift. Rather they are affected by uplift across the opposing submarine border faults and regional Peloponnesus uplift above the subducting African Plate (e.g. Leeder *et al.* 2003). Similarly, the model of Armijo *et al.* (1996) greatly over predicts (5 km versus 2.5 km observed) the maximum total sediment thickness in the main basin north of the Xylocastro fault (Fig. 12).

8 HORIZONTAL EXTENSION

We estimate the horizontal extension across the seismically imaged portion of the Gulf (Fig. 13) by measuring the across-strike widths of the basement fault polygons and summing them along each MCS line (Fig. 12)—whose trend is approximately orthogonal to structure. These are minimum estimates because not all fault offsets may be recognized in the MCS profiles. Minimum values for the nearshore/onshore portions of the Heliki, Akrata-Derveni and Xylocastro faults bordering our survey were estimated using their fault surface traces and approximate widths because we cannot determine their downdip extents and hanging wall basement intersections.

We measure 2–10 km of offshore extension across the GoC, varying along strike and by sector (Fig. 12). For example, measured

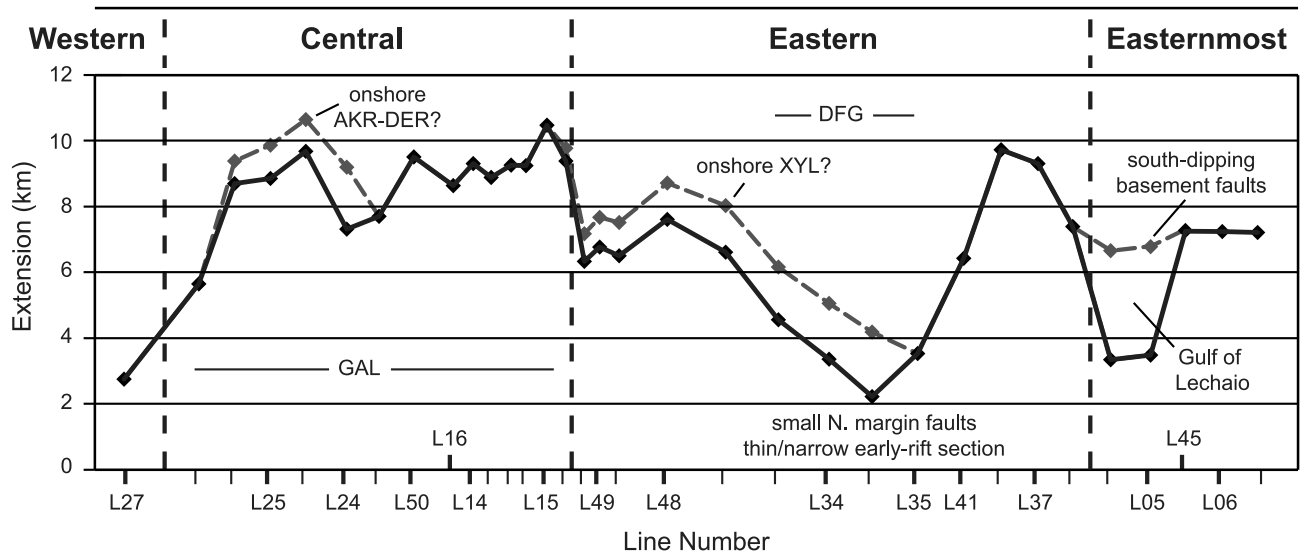


Figure 13. Estimated total horizontal component of submarine extension measured using fault polygon widths for each EW0108 MCS line (black line and diamonds). Extension estimates for the onshore portions of the Akrata-Derveni and Xylocastro faults are in grey. They represent minimum estimates because the downdip intersection of the fault with basement in the hanging wall is poorly constrained.

offshore extension is low in the western sector (~3 km) where the basement dips north into the axial West Channel Fault without apparent influence from the downdip portion of the Heliki fault (e.g. L27, Fig. 5; see also Bell *et al.* 2009). Topography (Fig. 3) shows that footwall uplift increases to the west on the Heliki fault, where the crossing antecedent (Vouraikos) river has deposited a large Gilbertfan delta on its hanging wall. However heave apparently decreases westward, associated with fault dip increasing from biplanar 35° to 15° in the central sector to high angle (~50°) in the west, such that our MCS data do not approach close enough to shore to image the downdip portion of the Heliki fault there. Numerous overlapping, high-angle normal faults further south, now inactive, may account for ~4 km of additional N–S extension, making ~7 km in total in the western sector.

The significantly greater offshore horizontal extension (8–10 km) measured in the central sector (Fig. 13) coincides with deepening and widening of the submarine basin, eastward crustal thinning, and the transition from the Pindos to Panassos basement nappes. Roughly two thirds of this extension derives from the wide fault polygons associated with the biplanar (including low-angle, 15–20°) southern border faults (Helike and Akrata-Derveni) and one third from the northern margin faults including the shallow-angle (25–34°) early rift Galaxidi fault and high-angle (50–65°) late-rift faults (Figs 10 and 12). The apparent extension minima measured near L24 (Fig. 13) corresponds to the structural ramp and overlap zone between the Heliki and Akrata-Derveni faults.

The eastern sector lacks large northern margin faults comparable to the Galaxidi fault, resulting in a decrease in the measured extension. This is where the early-rift sequence is thin and where motion on the Sithas fault has replaced that on the onshore portion of the Xylocastro fault during late-rift deposition. Total extension decreases from west to east where the Derveni fault departs the southern margin and the hanging-wall basement of the overlapping Sithas fault has not pulled off from its high-angle portion near the seafloor onto the low-angle, intrabasement portion. The large increase in total horizontal extension east of the Sithas fault corresponds to the offshore portion of the Xylocastro fault, which is low-angle near the base of the synrift section, and the transition

from a basin with small mid-basin faults and a thin early-rift section, to a basin with large faults and a substantially thicker early-rift section (compare L41, Fig. 7 with L37, Fig. 8).

The conservative extension estimates across the onshore portion of the Xylocastro fault are likely underestimates. The downdip extent of the fault is obscured by rift-related sediment and not well constrained from field mapping. Additionally, ~1 km of footwall topography is created across the eroded crests of onshore segments of the Xylocastro fault, a thick series of synrift sediments accumulated during hanging wall subsidence, and these are uplifted and incised by a marine terrace (Armijo *et al.* 1996; Flotte *et al.* 2005; Place *et al.* 2007). A more complete accounting of extension across the subaerial and nearshore segments of the Xylocastro fault may result in magnitudes of extension across the eastern sector more comparable to those measured across the central sector. Nevertheless, the thinner sediment thicknesses and shallower depths to basement on L35 and L41 (Fig. 12) attest to real differences in the amount of extension along strike and a minimum in that region of the eastern sector (Fig. 13). Yet we do not observe transfer faults in strike lines across the region (e.g. L09 and L19, Fig. 9), and do not know how the differential extension is accommodated.

Although similar amounts of extension (~6–7 km) are measured on L45 and L06 in the easternmost sector, they have some differing contributions: the Perahora Fault on L06 versus the south-dipping faults in the Gulf of Lechaio on L45 (Fig. 12). We extrapolate the offsets of the latter westward on L05 (and L38) though that line does not extend as far south to fully image the faults controlling the >2 km of sediment in the Gulf of Lechaio (Fig. 12). The thinner (<30 km) crust beneath the Perahora Peninsula (Zelt *et al.* 2005) is not explained by our extension estimates, suggesting that some of the variations in crustal thickness, especially in the easternmost sector, reflect the earlier Miocene, rather than the Plio-Pleistocene, phase of extension.

Notwithstanding considerable pre-rift topography, a comparison of Fig. 3 with Fig. 12 shows that, with one notable exception, the bathymetry is a good reflection of the differential creation of accommodation space accompanying Corinth rift extension. The exception is the semi-enclosed Gulf of Lechaio, where >2.5 km

of basement subsidence largely is masked by the thick sediments. Elsewhere, sedimentation has not kept pace with the axial rift subsidence, and channels erode the margins of the modern depocentre that is at 700–880 mbsl.

9 DISCUSSION AND CONCLUSIONS

To first order, the Corinth rift may be described as part of an extensional relay that links the Anatolian strike-slip faults to the Kefalonia Fault, forming part of the NW boundary of the Aegean microplate that advances southwards with the retreat of the subducting Tethyan slab (Fig. 1). The rift obliquely transects the Aegean forearc and Hellenic mountains, unlike the Oligo-Miocene extension systems that collapsed the alpine nappe stack in the Aegean arc/backarc. With the active extension focused offshore beneath the Gulf, the structural style of Corinthian rifting has been controversial, with competing models of high- versus low-angle, as well as bimodal, faulting. Our new data reveal the offshore fault geometry and seismic stratigraphy, allowing direct tests of various models and their predictions.

In the area of our marine survey, four active, right-stepping, en-echelon, N-dipping border fault systems trend ESE along the southern Gulf margin (Heliki, Derveni, Sithas and Xylocastro) and significantly overlap along strike; a fifth (Perahora) trends NE and does not overlap, stopping just west of the tip of the Peninsula (Figs 2 and 11). This contrasts with the Armijo *et al.* (1996) thick elastic plate model for rift-flank uplift of the Corinthian terraces, which posits a continuous high-angle, north-dipping, normal fault across the mouth of the Gulf of Lechaio and predicts a sediment thickness beneath the GoC of 5 km, neither of which are observed.

The offshore Heliki, Xylocastro and Derveni faults extend onshore westwards (Fig. 2). The basement offsets of the Akrata-Derveni, Sithas and Xylocastro faults are linked (Fig. 12). A basement splay of the Derveni fault further overlaps the Sithas fault to the north and subtends a late-rift graben that hosts the maximum thickness of the 3rd LRS sequence (L34, Fig. 7). Post-migration, depth converted EW0108 data confirm that all five southern margin normal fault systems are biplanar to listric: typically intermediate angle ($\sim 35^\circ$ in the central sector and $45\text{--}48^\circ$ in the east) near the surface/seafloor but decreasing in dip and/or intersecting a low- or shallow-angle ($15\text{--}20^\circ$ in the central sector and $19\text{--}30^\circ$ in the east) curvi-planar reflector in the basement (Fig. 10).

Major S-dipping border faults were active along the northern margin of the central Gulf early in the rift history (Galaxidi fault, current dip $25\text{--}38^\circ$), and remain active in the western Gulf (West Channel Fault, 50°) and in the subsidiary Gulf of Lechaio (Loutraki fault, $45\text{--}50^\circ$). Unlike the N-dipping border faults along the southern margin, the S-dipping border faults along the northern margin are without major footwall uplift. The fault geometries require that some of the large opposed (N- versus S-dipping) faults repeatedly cut one another in the basement (e.g. L25, L15 and L37, Fig. 10).

Noting the large north- and south-dipping early rift faults (in the central sector) Moretti *et al.* (2003) proposed a quasi-symmetric evolution of the central and eastern rift, only becoming more asymmetric with the recent localization of depocentres in the south. Our greater coverage and successive sequence isopachs (Fig. 11) show that the asymmetry is present from the beginning in the eastern sector and develops from early in the late rift (1st and 2nd sequences) in the central sector. Then, linkage of a high-angle, south-dipping normal fault, trending 276° from the Vrachonisida islands across the

eastern sector, permitted quasi-symmetric subsidence of the southern half of that sector during the latest rifting (3rd sequence, Fig. 11). Note that the higher dip of the Vrachonisida fault than the southern border faults means that even symmetric rift axis subsidence would equate to asymmetric extension, requiring greater heave on the shallower-dipping faults in the south to achieve equivalent throw to the those in the north.

Two other examples of late-rift fault growth are the formation of crestal collapse graben where the hanging wall has pulled off the steeper onto the shallower downdip segments of the Derveni Fault (Fig. 6; also see Sachpazi *et al.* 2003) and the formation of the Derveni Fault Graben (DFG, Fig. 7) above the eastern basement splay of the Derveni Fault (Figs 11 and 12). In contrast, the mid-basin sag (near the L19 crossing of L05 and L45, Fig. 7) that straddles the eastern/easternmost sector boundary attests to deep extension without a clear shallow fault expression. Note that the dominant strikes of the Corinth rift faults gradually rotate from ESE ($090\text{--}120^\circ$) in the basement and early rift to more E–W ($090\text{--}100^\circ$) in the latest rift (Fig. 11), reflecting a $\sim 10^\circ$ rotation of the opening direction to the 005° presently measured by GPS between Central Greece and the Peloponnesus Peninsula (Fig. 1 inset; Avallone *et al.* 2004; Nyst & Thatcher 2004).

Most major faults imaged by the EW0108 data were established early, probably initiating when the area was subaerial. There is little evidence in the marine data for lateral growth of the large border faults, though it may have occurred before there was a sedimentary record. However, migration of activity across established basement faults has occurred in a number of locations. Some mid-basin basement faults and the large early-rift Galaxidi fault have become inactive and/or were superceded by higher-angle late-rift faults, particularly in the central sector. During early-rift sedimentation, the Pirgaki-Mamousia (P-M, Fig. 2) fault and the onshore portions of the Xylocastro and Akrata-Derveni faults were active and sediment temporally equivalent to the early-rift section is present on their hanging walls. The significant sediment deposition and early-rift footwall uplift that occurred south of the modern Gulf shoreline was accompanied by motion on N- and S-dipping submarine faults to the north. The subaerial portions of the southern margin faults are now inactive and focused extension and accompanied footwall uplift has migrated northwards to the Heliki and Sithas faults and eastwards to the offshore portions of the Derveni and Xylocastro faults. The Eratini late-rift faults widened the submarine depocentre north of the West Channel Fault in the western sector (Figs 5 and 11), though by an amount significantly less than the northward migration of active faults on the Peloponnesus Peninsula (e.g. Ori 1989; Flotte *et al.* 2005; Ford *et al.* 2007; Rohais *et al.* 2007). Widening of the submarine depocentre is not observed in the central and eastern sectors (e.g. Figs 5–8 and 10). The net result has been a narrowing and focusing of Corinth rift extension to the offshore.

Sorel (2000) and Flotte *et al.* (2005) proposed that the high-angle normal faults in the western sector ride on a north-dipping detachment that roots in the shallow-dipping microseismicity zone of Rigo *et al.* (1996). Moretti *et al.* (2003), McNeil *et al.* (2005) and Bell *et al.* (2008, 2009) contend that such a detachment is not required to explain their observations of the variably symmetric offshore shallow structures and stratigraphy. However our deeper-penetrating MCS data reveal low- and shallow-angle southern border faults linked in the basement, even though the faults near-surface dips are higher angle (Fig. 10). Like the Sachpazi *et al.* (2003) first publication of deeply penetrating MCS data, our profiles allow the presence of one or more north-dipping detachment(s), down into which higher-angle faults sole (e.g. L48, Fig. 7), though they can

be explained also by linked biplanar to listric normal faults without a detachment (Fig. 10).

The debate will continue in part because, despite recording data to 16 s two-way traveltimes, deeper fault imaging with our large source and long streamer seismic reflection system was frustrated by the faults loss of seismic reflectivity within the basement above the 4–14-km deep seismogenic zone (Fig. 14). A first order seismogenic asymmetry of the western, central and eastern sectors is evident by the greater depths of (micro)seismicity (Fig. 14) and the location of all large Corinth rift earthquakes under the northern rift margin (Fig. 3), whereas the active border faults are mainly along the south coast (Figs 2 and 10–12). However the detailed relationship of the seismicity to the faults in the brittle upper crust remains undetermined by direct imaging.

In the western sector, for example, a definitive connection between imaged faults and large ($M_b \geq 5$) earthquake focal mechanisms and micro-earthquakes from Rigo *et al.* (1996) (or Gautier *et al.* 2006) is not apparent (Fig. 14). We image no low-angle intrabasement structures although micro-earthquakes from this region

have been cited as evidence for an active low-angle detachment at a depth of 8–10 km (Rietbrock *et al.* 1996; Rigo *et al.* 1996; Gautier *et al.* 2006). It has also been suggested that the earthquakes are related to the conjugate high-angle focal mechanism nodal planes but the geometry, location, and downdip continuity of the south-dipping faults imaged in L27 suggests not.

In the central sector, the imaged portions of the Heliki and Derveni faults are low-angle ($15\text{--}20^\circ$) in the basement and 1.5–2 km above a 15° -northward-dipping interface identified by Pi Alperin *et al.* (2004) using refracted active-source seismic wave arrivals from the EW0108 seismic air-gun source recorded by a codeployed land seismometer array (Fig. 14). Pi Alperin *et al.* (2004) suggest the interface represents a portion of the detachment fault proposed by Sorel (2000). Downdip extrapolations of both the interface and the faults pass close to the 1992, 1970 and 1965 earthquake focal mechanisms, but their nodal planes, respectively, dip 30° , 23° and 34° to the north, steeper than either the interface or the intrabasement border faults. Furthermore, the imaged low-angle faults in the central sector and the downdip extrapolation of the Sorel (2000)

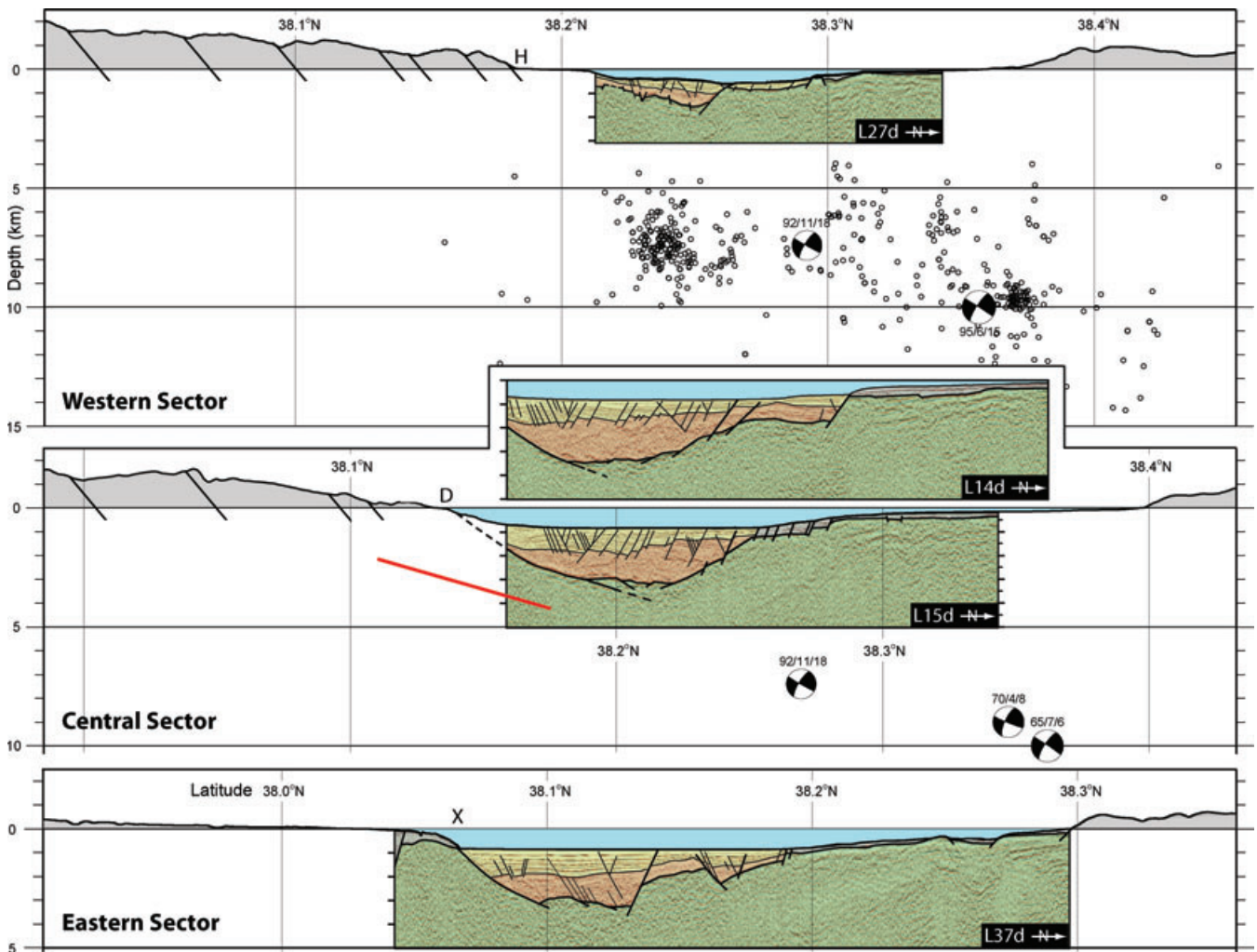


Figure 14. Topographic profiles overlain on interpreted depth-converted MCS data for the western (top panel), central (middle panel) and eastern (bottom panel) GoC rift sectors referred to in the text. Profile locations are shown in Fig. 2. Subaerial faults are shown extending to a depth of 0.5 km beneath sea level with a constant dip of 50° . Microseismicity data from Rigo *et al.* (1996) are projected onto the top panel using a 10-km half width. Select large earthquake focal mechanisms (also shown in Fig. 3) are projected onto the profiles. The solid red line on the middle panel indicates the approximate position of the shallow (15°) north-dipping interface determined by Pi Alperin *et al.* (2004) using refracted wave arrivals from the EW0108 seismic air-gun source. H, Heliki fault; D, Derveni fault; X, Xylocastro fault.

detachment are too shallow to be related to the dipping plane defined by the microseismicity in the western sector at 8–10 km (Rigo *et al.* 1996; Gautier *et al.* 2006).

No large earthquakes or microseismicity have been recorded across the part of the eastern sector east of Antikyra where the Sithas and Xylocastro faults are also biplanar or listric and shallow-angle (20–30°) down-dip in the basement (Fig. 10). For the 1981 earthquake sequence in the easternmost sector beneath the Gulf of Alkyonoides (Fig. 3) a biplanar and antithetic fault geometry was proposed, with the inferred deep-seated, shallow angle (~24°), normal fault being aseismic (King *et al.* 1985).

The potential for low-strength layers and/or detachments to influence the evolution of rifting through a pre-existing stack of nappes has been numerically modelled (Le Pourhiet *et al.* 2004; Le Pourhiet *et al.* 2006). Depending on the strength contrasts used, high-angle faults may root on multiple low-strength levels in addition to the brittle–ductile transition. Ghisetti & Vezzani (2004, 2005) propose that a structural high referred to as the Zaroukla culmination (ZC) acts as a north-trending mechanical barrier that segments the southern margin synrift sediments into thinner western (Aigion) and thicker eastern (Derveni-Xylocastro) subbasins and extends offshore as a submerged ridge between Galaxidi and Akrata (Fig. 3). They attribute the variable depth to the seismogenic zone and the maximum length of faults on either side of the basement culmination to different depths of a detachment at the top of the Phyllite-Quartzite nappe (Fig. 2). However, the proposed offshore extension of the ZC is in the same location as the deepest basement and thickest synrift section, we image no north-trending seafloor or basement ridge south of the Galaxidi Peninsula, and both the Akrata-Derveni and Galaxidi faults clearly cross the proposed barrier to fault propagation (Figs 11 and 12).

The same detachment was correlated across the Peloponnese Peninsula to the SSE as a major Miocene basin-bounding fault and termed the East Peloponnese Detachment by Papanikolaou & Royden (2007). They inferred that it controlled much of the subsidence and early sedimentation in the Corinth rift, which our EW0108 data clearly refute (Fig. 12). Subsequently, Papanikolaou *et al.* (2009) identified the mid-Miocene 25–40°-E-dipping Itea-Amfissa detachment, which passes through Galaxidi (Figs 2 and 3), as the northern continuation of the East Peloponnese Detachment and recognized, as we do, that it pre-dated the east-trending Corinth rift structures, by which it is cut.

As explained by Jolivet *et al.* (2010), the detachment mapped by Sorel (2000), the Zaroukla decollement near the base of the Gavrovo-Tripolitsa carbonates (that indicates northerly extension), lies above the East Peloponnese (a.k.a. Cretan) detachment at the top of the metapelitic Phyllite-Quartzite nappe (that has NE stretching lineations). Furthermore, the high-angle Tsivlos Fault (Fig. 2) cuts the former and may root on the latter (see Figs 5 and 6 in Jolivet *et al.* 2010). Their Fig. 6 is a composite section that combines features from the western and central sectors (Helike and Aigion faults and western microseismicity, versus Zaroukla-Tsivlos faults and central seismic section offshore). In contrast, our results indicate that the structural architectures of the western and central sectors are fundamentally different (Fig. 14), as also recognized for different reasons by Ghisetti & Vezzani (2005).

Jolivet *et al.* (2010) go on to speculate that the post-orogenic detachments of the Cyclades may provide good analogues for the deformation active below the GoC at the depth of the brittle–ductile transition. In our view, however, the Corinth Rift stands in marked contrast to the Cyclades, Colorado and Papua New Guinea metamorphic core complexes that formed in arc/backarc terranes with

elevated heat flow and syn-rift magmatism (e.g. Lister & Baldwin 1993). The thermally cool forearc setting and cross-orogen structures unaccompanied by magmatism make the Corinth Rift a poor analogue and unlikely precursor for metamorphic core complex formation.

The NNW structural grain of the Pindos zone parallels the dominant trend of the Hellenide nappe stack through central Greece and is highly oblique to the strike of normal faults (Figs 1 and 2). In contrast, the basement structural fabric is aligned ESE uniquely in the Parnassos zone, pre-conditioning the structural grain of the basement of the central and eastern GoC (Fig. 2). The fabric is nearly fault parallel where the GoC is widest, where faulting is concentrated offshore, where measured horizontal extension is large, and where the crust is thinner than that of the Hellenides. The transition from the Pindos to the Parnassos zone across their suture along the northern margin (Fig. 2) coincides with the western-central sector boundary, the eastward deepening Gulf floor and top of basement. Likewise, the transition from the Parnassos to the Pelagonian nappe in the east coincides with transition to the Alkyonides Gulf across a basement culmination. We oversimplify the complexity of the nappe stack in Fig. 2 but suggest that the change in orientation of nappe structural fabric pre-conditions the basement, and may control the geometry and position of large normal faults across the central and eastern sectors. The alignment of the inherited basement structure bordering the Parnassos is likely a significant factor in the localization of the GoC.

The relatively shallow dips of the intrabasement portions of the southern border faults and their listric or biplanar geometries do not definitively indicate the presence of an active detachment fault. The low-angle faults might detach at shallow levels in the upper crust and not directly link to the seismogenic zone. The basement beneath the GoC is heterogeneous. We infer that potential slip surfaces along sutures, bedding planes and weak lithologies within the nappe stack act as detachments and play an important role in strain partitioning. This complexity may be why deep, continuous, seismogenic faults are so difficult to image beneath the GoC, leaving one tempted to draw lines through clouds of micro-earthquakes. Despite our inability to image faults extending into the seismogenic zone, we have shown that, except possibly in the western sector, the southern margin faults do not maintain a high-angle through the upper crust.

Based on our observations, we propose the following simple structural model for the Corinth rift. In the central and eastern sectors, multiple, subparallel, low-angle interfaces inherited from the structural fabric associated with the Parnassos nappe stack are being reactivated in the basement, with higher-angle faults linking them to each other and, via listric to biplanar faults, to the surface. In contrast, in the western sector the structural fabric of the thick orogenic crust and Pindos nappe stack is at a high angle to the Corinth rift axis. Without favorably oriented pre-existing basement fabric, a broader zone of high-angle faults developed there. Whether they detach at depth in a fault or ductile zone remains to be determined. The greater total offshore extension of the central and eastern sectors is now being complemented by focused extension that GPS data confirm is occurring at increasing rates along strike in the western sector.

ACKNOWLEDGMENTS

This project was conceived by, and funded by grants to BT (U.S. National Science Foundation), AH and MS. All authors participated in the R/V Maurice Ewing cruise, ably assisted by Aris Stefatos, Masako Fujimoto, Barry Taylor and Barry Zelt. AG and JW

completed the post-cruise processing of the MCS data in the lab of Gregory Moore. JW processed the multibeam bathymetry data. Interpretation of the data and the writing of this paper were led by BT and JW. We thank the officers, crew and technicians of the R/V Maurice Ewing, and the Hellenic Coast Guard for picket boat services, for collecting quality long-streamer MCS data in the narrow GoC. This is SOEST contribution #8,091.

REFERENCES

- Abers, G.A., 2001. Evidence for seismogenic normal faults at shallow dips in continental rifts, in *Non-Volcanic Rifting of Continental Margins: A Comparison of Evidence from Land and Sea*, pp. 305–318, eds Wilson, R.C.L., Whitmarsh, R.B., Taylor, B. & Frotzheim, N., Geol. Soc. Lond. Spec. Pub.
- Ambraseys, N.N. & Jackson, J., 1990. Seismicity and associated strain of central Greece between 1890 and 1988, *Geophys. J. Int.*, **101**, 663–708.
- Armijo, R., Meyer, B., King, G.C.P., Rigo, A. & Papanastassiou, D., 1996. Quaternary evolution of the Corinth Rift and its implications for the Late Cenozoic evolution of the Aegean, *Geophys. J. Int.*, **126**, 11–53.
- Aubouin, J. *et al.*, 1970. Contribution a la geologie des Hellenides: le Garvrovo, le Pinde et la zone ophiolitique supelagonienne, *Ann. Soc. Geol. Nord*, **90**, 277–306.
- Avallone, A. *et al.*, 2004. Analysis of eleven years of deformation measured by GPS in the Corinth Rift Laboratory area, *Comptes Rendus Geosci.*, **336**, 301–311.
- Backert, N., Ford, M. & Malartre, F., 2010. Architecture and sedimentology of the Kerinitis Gilbert-type fan delta, Corinth Rift, Greece, *Sedimentology*, **57**, 543–586.
- Bell, R.E., McNeill, L.C., Bull, J.M. & Henstock, T.J., 2008. Evolution of the offshore western Gulf of Corinth, *Geol. Soc. Am. Bull.*, **120**, 156–178.
- Bell, R.E., McNeill, L.C., Bull, J.M., Henstock, T.J., Collier, R.E.L. & Leeder, M.R., 2009. Fault architecture, basin structure and evolution of the Gulf of Corinth Rit, central Greece, *Basin Res.*, **21**, 824–855.
- Bernard, P. *et al.*, 1997. The Ms = 6.2, June 15, 1995 Aigion earthquake (Greece): evidence for low angle normal faulting in the Corinth rift, *J. Seismol.*, **1**, 131–150.
- Bintanja, R. & van de Wal, R.S.W., 2008. North American ice-sheet dynamics and the onset of 100,000-year glacial cycles, *Nature*, **454**, 869–872.
- Braunmiller, J. & Nabelek, J., 1996. Geometry of continental normal faults: seismological constraints, *J. geophys. Res.*, **101**, 3045–3052.
- Briole, P. *et al.*, 2000. Active deformation of the Corinth rift, Greece: results from repeated Global Positioning System surveys between 1990 and 1995, *J. geophys. Res.*, **105**, 25605–25625.
- Brooks, M. & Ferentinos, G., 1984. Tectonics and sedimentation in the Gulf of Corinth and the Zakynthos and Kefallinia channels, western Greece, *Tectonophysics*, **101**, 25–54.
- Causse, C., Moretti, I., Eschard, R., Micarelli, L., Ghaleb, B. & Frank, N., 2004. Kinematics of the Corinth Gulf inferred from calcite dating and syntectonic sedimentary characteristics, *Comptes Rendus Geosci.*, **336**, 281–290.
- Clement, C., 2000. Imagerie sismique crustale de la subduction Hellenique et du Golfe de Corinth, *PhD thesis*, University Paris VII, Paris.
- Clement, C., Sachpazi, M., Charvis, P., Graindorge, D., Laigle, M., Hirn, A. & Zafropoulos, G., 2004. Reflection-refraction seismics in the Gulf of Corinth: hints at deep structure and control of the deep marine basin, *Tectonophysics*, **391**, 97–108.
- Collier, R.E.L., Leeder, M.R., Rowe, P.J. & Atkinson, T.C., 1992. Rates of tectonic uplift in the Corinth and Megara Basins, central Greece, *Tectonics*, **11**, 1159–1167.
- Collier, R.E.L., Leeder, M.R., Trout, M., Ferentinos, G., Lyberis, E. & Papatheodorou, G., 2000. High sediment yields and cool, wet winters: test of last glacial paleoclimates in the northern Mediterranean, *Geology*, **28**, 999–1002.
- Doan, M.L. & Cornet, F.H., 2007. Thermal anomaly near the Aigio fault, Gulf of Corinth, Greece, maybe due to convection below the fault, *Geophys. Res. Lett.*, **34**, L06314, doi:06310.101029/02006GL028931.
- Doutsos, T. & Piper, D.J.W., 1990. Listric faulting, sedimentation, and morphological evolution of the Quaternary eastern Corinth rift, Greece: first stages of continental rifting, *Geol. Soc. Am. Bull.*, **102**, 812–829.
- Ferentinos, G., Papatheodorou, G. & Collins, M.B., 1988. Sediment transport processes on an active submarine fault escarpment: Gulf of Corinth, Greece, *Mar. Geol.*, **83**, 43–61.
- Flotte, N., Plangnes, V., Sorel, D. & Benedicto, A., 2001. Attempt to date Pleistocene normal faults of the Corinth-Patras Rift (Greece) by U/Th method, and tectonic implications, *Geophys. Res. Lett.*, **28**, 3769–3772.
- Flotte, N., Sorel, D., Mueller, C. & Tensi, J., 2005. Along strike changes in the structural evolution over a brittle detachment fault: example of the Pleistocene Corinth-Patras rift (Greece), *Tectonophysics*, **403**, 77–94.
- Ford, M., Williams, E.A., Malartre, F. & Popescu, S.-M., 2007. Stratigraphic architecture, sedimentology and structure of the Vouraikos Gilbert-type delta, Gulf of Corinth, Greece, in *Special Publication of the International Association of Sedimentologists*, pp. 44–90, eds Paola, C., Nichols, G.J. & Williams, E.A. Blackwell Publishing, Malden, MA.
- Ford, M., Le Carlier de Veslud, C., Lyon-Caen, H., Rohais, S., Moullard, M. & Williams, E.A., 2008. Normal fault systems of the Western Corinth Rift (Greece): 3D geometry, kinematics, and evolution, *EOS, Trans. Am. geophys. Un.*, **89**, Fall Meet. Suppl., Abstract T43C-2056.
- Gautier, S., Latorre, D., Virieux, J., Deschamps, A., Skarpelos, C., Sotiriou, A., Serpetsidaki, A. & Tselentis, A., 2006. A new passive tomography of the Aigion area (Gulf of Corinth, Greece) from the 2002 data set, *Pure appl. Geophys.*, **163**, 431–453.
- Gawthorpe, R.L., Fraser, A.J. & Collier, R.E.L., 1994. Sequence stratigraphy in active extensional basins: implications for the interpretation of ancient basin-fills, *Mar. Petrol. Geol.*, **11**, 642–658.
- Ghisetti, F. & Vezzani, L., 2004. Fault segmentation in the Gulf of Corinth (Greece) constrained by patterns of Pleistocene sedimentation, *Comptes Rendus Geosci.*, **336**, 243–249.
- Ghisetti, F. & Vezzani, L., 2005. Inherited structural controls on normal fault architecture in the Gulf of Corinth (Greece), *Tectonics*, **24**, TC4016, doi:4010.1029/2004TC001696.
- Goldsworthy, M. & Jackson, J., 2001. Migration of activity within normal fault systems: examples from the Quaternary of mainland Greece, *J. Struct. Geol.*, **23**, 489–506.
- Goldsworthy, M., Jackson, J. & Haines, J., 2002. The continuity of active fault systems in Greece, *Geophys. J. Int.*, **148**, 596–618.
- Hatzfeld, D., Karakostas, V., Ziazia, M., Kassaras, I., Papadimitriou, E., Makropoulos, K., Voulgaris, N. & Papaioannou, C., 2000. Microseismicity and faulting geometry in the Gulf of Corinth (Greece), *Geophys. J. Int.*, **141**, 438–456.
- Heezen, B.C., Ewing, M. & Johnson, G.L., 1966. The Gulf of Corinth floor, *Deep-Sea Res.*, **13**, 381–411.
- Higgs, B., 1988. Syn-sedimentary structural controls on basin deformation in the Gulf of Corinth, Greece, *Basin Res.*, **1**, 155–165.
- Hinsbergen, D.J.J.v., Langereis, C.G. & Meulenkamp, J.E., 2005. Revision of the timing, magnitude and distribution of Neogene rotations in the western Aegean region, *Tectonophysics*, **396**, 1–34.
- Houghton, S.L., Roberts, G.P., Papanikolaou, I.D., McArthur, J.M. & Gilmour, M.A., 2003. New 234U-230U coral dates from the western Gulf of Corinth: implications for extensional tectonics, *Geophys. Res. Lett.*, **30**, 2013–2016.
- Jackson, J.A., Gagnepain, J., Houseman, G., King, G.C.P., Papadimitriou, P., Soufleris, C. & Virieux, J., 1982. Seismicity, normal faulting, and the geomorphological development of the Gulf of Corinth (Greece): the Corinth earthquakes of February and March 1981, *Earth planet. Sci. Lett.*, **57**, 377–397.
- Jacobshagen, V., Durr, S., Kockel, F., Kopp, K.O. & Kowalczyk, G., 1978. Structure and geodynamic evolution of the Aegean region, in *Alps, Apennines, Hellenides*, pp. 538–564, eds Cloos, H., Roeder, D. & Schmidt, K. E., Schweizerbart'sche Verlagsbuchhandlung, Stuttgart, Germany.
- Jolivet, L. & Faccenna, C., 2000. Mediterranean extension and the Africa-Eurasia collision, *Tectonics*, **19**, 1095–1106.
- Jolivet, L., Rimmelé, G., Oberhänsli, R., Goffé, B. & Candan, O., 2004. Correlation of syn-orogenic tectonic and metamorphic events in the Cyclades,

- the Lycian nappes and the Menderes massif. Geodynamic implications, *Bull. Soc. Geol. France*, **175**, 217–238.
- Jolivet, L., Labrousse, L., Agard, P., Lacombe, O., Bailly, V., Lecomte, E., Mouthereau, F. & Mehl, C., 2010. Rifting and shallow-dipping detachments, clues from the Corinth Rift and the Aegean, *Tectonophysics*, **483**, 287–304.
- Keraudren, B. & Sorel, B., 1987. The terraces of Corinth (Greece)-A detailed record of eustatic sea level variations during the last 500,000 years, *Mar. Geol.*, **77**, 99–107.
- King, G.C.P. et al., 1985. The evolution of the Gulf of Corinth (Greece) an aftershock study of the 1981 earthquakes, *Geophys. J. Roy. astr. Soc.*, **80**, 677–693.
- Kiratzi, A. & Louvari, E., 2003. Focal mechanisms of shallow earthquakes in the Aegean Sea and the surrounding lands determined by waveform modelling: a new database, *J. Geodyn.*, **36**, 251–274.
- Le Pichon, X., Chamot-Rooke, N., Lalleman, S., Noomen, R. & Veis, G., 1995. Geodetic determination of the kinematics of central Greece with respect to Europe: implications for eastern Mediterranean tectonics, *J. geophys. Res.*, **100**, 12 675–12 690.
- Le Pourhiet, L., Burov, E. & Moretti, I., 2003. Initial crustal thickness geometry controls on the extension in a back arc domain: case of the Gulf of Corinth, *Tectonics*, **22**, 1032, doi:10.1029/2002TC001433.
- Le Pourhiet, L., Burov, E. & Moretti, I., 2004. Rifting through a stack of inhomogeneous thrusts (the dipping pie concept), *Tectonics*, **23**, TC4005, doi:10.1029/2003TC001584.
- Le Pourhiet, L., Mattioni, L. & Moretti, I., 2006. 3D modeling of rifting through a pre-existing stack of nappes in the Gulf of Corinth (Greece): a mixed analogue/numerical approach, *Geol. Soc. Lond. Spec. Publ.*, **253**, 233–252.
- Leeder, M.R. & Mack, G.H., 2007. Basin-fill incision, Rio Grande and Gulf of Corinth rifts: convergent response to climatic and tectonic drivers, in *Sedimentary Processes, Environments and Basins*, pp. 9–28, eds Nichols, G., Williams, E. & Paola, C., Blackwell Publishing, Malden, MA.
- Leeder, M.R., Harris, T. & Kirby, M.J., 1998. Sediment supply and climate change: implications for basin stratigraphy, *Basin Res.*, **10**, 7–18.
- Leeder, M.R., McNeil, L.C., R.E.L., C., Portman, C., Rowe, P.J., Andrews, J.E. & Gawthorpe, R.L., 2003. Corinth Rift margin uplift: new evidence from Late Quaternary marine shorelines, *Geophys. Res. Lett.*, **30**, doi:10.1029/2003GL017382.
- Leeder, M.R. et al., 2005. Normal faulting and crustal deformation, Alkyonides Gulf and Perachora peninsula, eastern Gulf of Corinth rift basin, Greece, *J. geol. Soc. Lond.*, **162**, 549–561.
- Leeder, M.R., Mack, G.H., Brasier, A.T., Parish, R.R., McIntosh, W.C., Andrews, J.E. & Durmeijer, C.E., 2008. Late-Pliocene timing of Corinth (Greece) rift-margin fault migration, *Earth planet. Sci.*, **274**, 132–141.
- Lister, G.S. & Baldwin, S.L., 1993. Plutonism and the origin of metamorphic core complexes, *Geology*, **21**, 607–610.
- Lykousis, V., Sakellariou, D., Papanikolaou, D., 1998. Sequence stratigraphy in the northern margin of the Gulf of Corinth: implications to upper Quaternary basin evolution, *Bull. Geol. Soc. Greece*, **32**, 157–164.
- Lykousis, V., Sakellariou, D., Moretti, I. & Kaberi, H., 2007. Late Quaternary basin evolution of the Gulf of Corinth: sequence stratigraphy, sedimentation, fault-slip and subsidence rates, *Tectonophysics*, **440**, 29–51.
- Makris, J., 1978. A geophysical study of Greece based on deep seismic sounding, gravity and magnetics, in *Alps, Apennines, Hellenides*, pp. 392–401, eds Cloos, H., Roeder, D. & Schmidt, K.E., Schweizerbart'sche Verlagsbuchhandlung, Stuttgart, Germany.
- McClusky, S. et al., 2000. Global positioning system constraints on plate kinematics and dynamics in the eastern mediterranean and caucasus, *J. geophys. Res.*, **105**, 5695–5719.
- McKenzie, D., 1978. Active tectonics of the Mediterranean region, *Geophys. J. Roy. astr. Soc.*, **30**, 109–185.
- McNeil, L.C. & Collier, R.E.L., 2004. Uplift and slip rates of the eastern Eliki fault segment, Gulf of Corinth, Greece, inferred from Holocene and Pleistocene terraces, *J. Geol. Soc. Lond.*, **161**, 81–92.
- McNeil, L.C. et al., 2005. Active faulting within the offshore western gulf of Corinth, Greece: implications for models of continental rift deformation, *Geology*, **33**, 241–244.
- Mercier, J., Sorel, D., Vergely, P. & Simeakis, K., 1989. Extensional tectonic regimes in the Aegean basins during the Cenozoic, *Basin Res.*, **2**, 49–71.
- Moretti, I., Sakellariou, D., Lykousis, V. & Micarelli, L., 2003. The Gulf of Corinth: an active half graben?, *J. Geodyn.*, **36**, 323–340.
- Nyst, M. & Thatcher, W., 2004. New constraints on the active tectonic deformation of the Aegean, *J. geophys. Res.*, **109**, doi:10.1029/2003JB002830.
- Ori, G.G., 1989. Geologic history of the extensional basin of the Gulf of Corinth (?Miocene-Pleistocene), Greece, *Geology*, **17**, 918–921.
- Palyvos, N., Mancini, M., Sorel, D., Lemeille, F., Pantosti, D., Julia, R., Triantaphyllou, M. & Martini, P.-M.d., 2010. Geomorphological, stratigraphic and geochronological evidence of fast Pleistocene coastal uplift in the westernmost part of the Corinth Gulf Rift (Greece), *Geol. J.*, **45**, 78–104.
- Papanikolaou, D., Gouliotis, L. & Triantaphyllou, M., 2009. The Itea-Amfissa detachment: a pre-Corinth rift Miocene extensional structure in central Greece, in *Collision and Collapse at the Africa-Arabia-Eurasia Subduction Zone*, pp. 293–310, eds Hinsbergen, D.J.J.v., Edwards, M.A. & Govers, R., The Geological Society, London.
- Papanikolaou, D.J. & Royden, L.H., 2007. Disruption of the Hellenic arc: late Miocene extensional detachment faults and steep Pliocene-Quaternary normal faults – Or what happened at Corinth?, *Tectonics*, **26**, TC5003, doi:10.1029/2006TC002007.
- Papastamatiou, J. & Tataris, A., 1963. Tectonics of the transitional sediments from the Parnassos-Giona unit to the Olonos-Pindos unit, *Bull. Geol. Soc. Greece*, **5**, 86–89.
- Papatheodorou, G. & Ferentinos, G., 1997. Submarine and coastal sediment failure triggered by the 1995, Ms = 6.1 Aegion earthquake, Gulf of Corinth, Greece, *Mar. Geol.*, **137**, 287–304.
- Papazachos, C. & Nolet, G., 1997. P and S deep velocity structure of the Hellenic area obtained by robust nonlinear inversions of travel times, *J. geophys. Res.*, **102**, 8349–8367.
- Pe-Piper, G. & Piper, D.J.W., 2002. *The Igneous Rocks of Greece: The Anatomy of an Orogen*, Gebrüder Borntraeger, Berlin.
- Perissoratis, C., Mitropoulos, D. & Angelopoulos, L., 1986. Marine geological research at the eastern Corinthiakos Gulf, *Geol. geophys. Res., Special Issue*, 381–401. IGME, Athens.
- Perissoratis, C., Piper, D.J.W. & Lykousis, V., 2000. Alternating marine and lacustrine sedimentation during late Quaternary in the Gulf of Corinth rift basin, central Greece, *Mar. Geol.*, **167**, 391–411.
- Philippson, A., 1892. *Der Peloponnes*, Vol., Verlag Friedlaender, Berlin.
- Pi Alperin, J.M., Marthelot, J.M., Galve, A., Sachpazi, M., Taylor, B., Laigle, M. & Hirn, A., 2004. Seismic refraction imaging of the southern Corinth rift shoulder at Derveni, *Comptes Rendus Geosci.*, **336**, 251–257.
- Piper, D.J.W., 2006. Sedimentology and tectonic setting of the Pindos Flysch of the Peloponnese, Greece, *Geol. Soc. Lond. Spec. Publ.*, **260**, 493–505.
- Pirazzoli, P., Stiros, S., Fontugne, M. & Arnold, M., 2004. Holocene and quaternary uplift in the central part of the southern coast of the Corinth Gulf (Greece), *Mar. Geol.*, **212**, 35–44.
- Place, J., Geraud, Y., Diraison, M. & Warr, L., 2007. North-south transfer zones and paleo-morphological reconstruction of the Xylocaastro area (Corinth Gulf, Greece), *Tectonophysics*, **440**, 121–139.
- Rietbrock, A., Tiberi, C., Scherbaum, F. & Lyon-Caen, H., 1996. Seismic slip on a low angle normal fault in the Gulf of Corinth: evidence from high-resolution cluster analysis of microearthquakes, *Geophys. Res. Lett.*, **23**, 1817–1820.
- Rigo, A., Lyon-Caen, H., Armijo, R., Deschamps, A., Hatzfeld, D., Makropoulos, K., Papadimitriou, P. & Kassaras, I., 1996. A microseismic study in the western part of the Gulf of Corinth (Greece): implications for large-scale normal fault mechanisms, *Geophys. J. Int.*, **126**, 663–688.
- Rohais, S., Eschard, R., Ford, M., Guillocheau, F. & Moretti, I., 2007. Stratigraphic architecture of the Plio-Pleistocene infill of the Corinth Rift: implications for its structural evolution, *Tectonophysics*, **440**, 5–28.
- Rohais, S., Eschard, R. & Guillocheau, F., 2008. Depositional model and stratigraphic architecture of rift climax Gilbert-type fan deltas (Gulf of Corinth, Greece), *Sediment. Geol.*, **210**, 132–145.
- Sachpazi, M., Clement, C., Laigle, M., Hirn, A. & Roussos, N., 2003. Rift structure, evolution, and earthquakes in the Gulf of Corinth, from reflection seismic images, *Earth planet. Sci. Lett.*, **216**, 243–257.

- Sachpazi, M. *et al.*, 2007. Moho topography under central Greece and its compensation by Pn time-terms for accurate location of hypocenters: the example of the Gulf of Corinth 1995 Aigion earthquake, *Tectonophysics*, **440**, 53–65.
- Sakellariou, D., Lykousis, V. & Papanikolaou, D., 1998. Neotectonic structure and evolution of the Gulf of Alkyonides, central Greece, *Bull. Geol. Soc. Greece*, **32**, 241–250.
- Sakellariou, D., Fountoulis, I. & Lykousis, V., 2004. Lechaion Gulf: the last descendant of the Proto-Gulf-of-Corinth basin, in *Proceedings of the 5th International Symposium on Eastern Mediterranean Geology*, pp. 881–884, Thessaloniki, Greece.
- Sakellariou, D., Lykousis, V., Alexandri, S., Kaberi, H., Rousakis, G., Nomikou, P., Georgiou, P. & Ballas, D., 2007. Faulting, seismic-stratigraphic architecture and Late Quaternary evolution of the Gulf of Alkyonides Basin-East Gulf of Corinth, Central Greece, *Basin Res.*, **19**, 273–295.
- Schwan, W., 1978. Structural tectonics of the Parnassus-Ghiona Mountains in the Central Hellenides, in *Alps-Apennines-Hellenides*, pp. 430–433, eds Closs, H., Roeder, D. & Schmidt, K., Schweizerbart, Stuttgart.
- Skourlis, K. & Doutsos, T., 2003. The Pindos Fold-and-thrust belt (Greece): inversion kinematics of a passive continental margin, *Int. J. Earth Sci.*, **92**, 891–903.
- Sorel, D., 2000. A Pleistocene and still-active detachment fault and the origin of the Corinth-Patras rift, Greece, *Geology*, **28**, 83–86.
- Stefatos, A., Papatheodorou, G., Ferentinos, G., Leeder, R. & Collier, R., 2002. Seismic reflection imaging of active offshore faults in the Gulf of Corinth: their seismotectonic significance, *Basin Res.*, **14**, 487–502.
- Taylor, B., Goodliffe, A.M. & Martinez, F., 1999. How continents break up: insights from Papua New Guinea, *J. geophys. Res.*, **104**, 7497–7512.
- Taymaz, T., 1992. Observations on source time functions of earthquakes obtained from inversion of teleseismic body waveforms, *Geophys. J. Int.*, **108**, 273–280.
- Taymaz, T., Jackson, J., & McKenzie, D., 1991. Active tectonics of the north and central Aegean Sea, *Geophys. J. Int.*, **106**, 433–490.
- Tiberi, C., Diament, M., Lyon-Caen, H. & King, T., 2001. Moho topography beneath the Corinth Rift area (Greece) from inversion of gravity data, *Geophys. J. Int.*, **145**, 797–808.
- Weiss, J.R., 2004. A Geophysical Investigation of the Gulf of Corinth, Greece, *MSc thesis*, University of Hawaii, Honolulu.
- Westaway, R., 2002. The Quaternary evolution of the Gulf of Corinth, central Greece: coupling between surface processes and flow in the lower continental crust, *Tectonophysics*, **348**, 269–318.
- Yilmaz, O., 2001. *Seismic Data Analysis*, Vol. 1, SEG, Tulsa, OK.
- Zelt, B.C., Taylor, B., Weiss, J.R., Goodliffe, A.M., Sachpazi, M. & Hirn, A., 2004. Streamer tomography velocity models for the Gulf of Corinth and Gulf of Itea, Greece, *Geophys. J. Int.*, **159**, 333–346.
- Zelt, B.C., Taylor, B., Sachpazi, M. & Hirn, A., 2005. Crustal velocity and Moho structure beneath the Gulf of Corinth, Greece, *Geophys. J. Int.*, **162**, 257–268.